Assessing the plausibility of direct constraints on ancient atmospheric P_{CO_2} from fluid inclusions in halite: A theoretical and experimental approach

Michael Naylor Hudgins[1,2], Justin G. Park[1,2], Alex M. Ryan[1,2], Jessika A. Rogers[3], and Morgan F. Schaller[1,2]*

[1]Department of Earth and Environmental Sciences, Rensselaer Polytechnic Institute, Troy, NY, USA.

[2]Center for Environmental and Stable Isotope Analysis, Rensselaer Polytechnic Institute, Troy, NY, USA.

[3]Department of Physics, Applied Physics, and Astronomy, Rensselaer Polytechnic Institute, Troy, NY, USA.

Abstract

Fluid inclusions in halite formed in surficial environments have recently gained attention for their ability to capture and preserve samples of ancient air, and by mechanical decrepitation, these inclusion gases can be quantified via mass spectrometry. However, it has yet to be demonstrated that the CO_2 content measured during bulk analysis of fluid inclusion gas on halite accurately represents the overlying air at various CO_2 concentrations and not the exsolution of some or all of the dissolved inorganic carbon. Based on the kinetics of the carbonate system and aqueous solubility of CO_2, we hypothesize that the CO_2 measured by bulk analysis of fluid inclusion gas is derived solely from a mixture between $CO_{2\,(g)}$ and $[CO_2]_{aq}$ (CO_2 from air and air-saturated brine). To address this, we first conducted depressurization experiments on atmospherically equilibrated carbonate solutions, and by mass balance we show that only $CO_{2(aq)}$ degasses during solution depressurization, while the remaining HCO_3^- and CO_3^{2-} combine with Na^+ cations to precipitate $NaHCO_3$ salt. In addition, we performed mechanical decrepitation experiments on lab-grown halite that was precipitated in a sealed pressure vessel under various CO_2 partial pressures (P_{CO2}; 450 ppm, 3000 ppm, and 5000 ppm). Volatile contents of the carbonate solutions and the lab-grown halite were analyzed with a quadrupole mass spectrometer. Measured CO_2 content falls between the expected values of air and air-saturated brine for the different P_{CO2} conditions, and by partitioning the contributions of the gaseous and aqueous phases, we observe atmospheric P_{CO2} that closely matches the starting conditions. Our findings demonstrate that fluid inclusions in halite faithfully entrap and preserve CO_2 from the overlying atmosphere and that the exsolution of DIC during decrepitation does not meaningfully contribute to the measured CO_2, giving confidence in applying our methods to new and existing analyses of both modern and ancient natural halite. Bulk gas analysis of fluid inclusions is one of the few methods to directly constrain ancient atmospheric composition through deep time and extend the record of atmospheric P_{CO2} well beyond the ice cores.

Keywords: Fluid Inclusions, Earth's Ancient Atmosphere, CO_2, Halite

*Corresponding author at: Department of Earth and Environmental Sciences, Rensselaer Polytechnic Institute, Troy, NY, USA. *Email address*: schall@rpi.edu

1. Introduction

Understanding Earth's climate history depends on reconstructing past atmospheric CO_2 concentrations, which relies on indirect geochemical proxies for time periods prior to the ice core record. (Petit et al., 1999; Schaller et al., 2015; CenCO2PIP, 2023). In ancient systems, proxy methods used to estimate atmospheric CO_2 partial pressure (P_{CO2}) often show similar trends over the same time interval, but disagree in absolute value (e.g., the $\delta^{13}C$ of pedogenic carbonates and leaf stomatal indices during the late Triassic; c.f. McElwain et al., 1999; Schaller et al., 2011). Despite these and similar inconsistencies, many of the proxy methods show the expected coherent relationship between relative P_{CO2} and temperature on geological timescales, indicating that they are precise but ultimately inaccurate (Knobbe and Schaller, 2018; Tierney et al., 2020; Judd et al., 2024). Addressing this inaccuracy requires direct constraints on ancient atmospheric CO_2, which can be accomplished using fluid inclusions hosted in halite that trap and preserve aliquots of ancient air and brine. Halite forms at the air-water interface in both modern and ancient surficial saline pan or similar closed-basin environments. Recent measurements have demonstrated that gases contained within the fluid inclusions in these halites are a direct and high-fidelity archive of Earth's atmospheric composition extending to time periods prior to the ice core record (Blamey et al., 2016; Steadman et al., 2020; Park and Schaller, 2025; Park et al., 2025). Gas analysis of inclusions in halite can be used to validate and refine existing CO_2 proxy records; however, because of the differences in aqueous solubility of the individual gases accurate interpretations of inclusion gases requires explicit consideration of phase chemistry (Park and Schaller, 2025).

Major atmospheric gases contained within fluid inclusions (e.g., N_2, O_2, Ar, and CO_2) can be quantified via mass spectrometry through mechanical decrepitation under high-vacuum (Graney and Kesler, 1995; Williams, 1996; Norman and Blamey, 2001; Pettitt and Schaller, 2020). Within the past decade, the gas compositions from Proterozoic and Phanerozoic halite have provided direct constraints on ancient atmospheric composition (Blamey et al., 2016; Steadman et al., 2020; Brand et al., 2021). However, these studies have garnered criticism for interpreting raw results (Yeung, 2017; Mills et al., 2023; Park and Schaller, 2025) that contradict prior model predictions and geochemical proxies (Lyons et al., 2014; Catling and Zahnle, 2020). A major issue with these studies is the failure to partition the gaseous from the aqueous phases in their analyses, as they explicitly assume that the volatiles measured are solely from air bubbles within the inclusions, neglecting the contribution of the aqueous phase. Ignoring the volatile contribution from the aqueous phase in inclusion analyses lead to erroneous interpretations of the overlying atmosphere (Park and Schaller, 2025), as the individual gaseous components of the atmosphere are notably different than the aqueous component at equilibrium, due to solubility differences (Yeung, 2017; Pettitt et al., 2020). Park and Schaller (2025) resolved this problem by developing a gas-aqueous partitioning method for fluid inclusion data to apportion the atmospheric volatiles between the gaseous and aqueous phases and determine the equilibrium atmosphere under which the sample had formed (see section 3.5 for more details). This method was validated through analyses of inclusions in halite grown under controlled laboratory conditions, where the partitioned gas data align with gas compositions of the known atmospheric condition (Park and Schaller, 2025). After a robust screening protocol for primary fluid inclusions (primary fluid inclusions form contemporaneously with the initial growth of the host crystal), this partitioning method can be applied to ancient halite to reconstruct ancient atmospheric CO_2 compositions, showing that the measured gas contents align well with existing models and proxies (Canfield, 2013; Krissansen-Totton et al., 2018; Park and Schaller, 2025). Furthermore, Park and Schaller (2025) demonstrated that only after applying the gas-aqueous partitioning method to Blamey et al's (2016) and Blamey's and Brand's (2019) data does the CO_2 content produce meaningful results, highlighting the necessity of applying the gas-aqueous correction to raw inclusion data.

The gas-aqueous partitioning method has changed how we interpret ancient atmospheric compositions from fluid inclusion data and our understanding of the biogeochemical cycling of atmospheric volatiles (Park and Schaller, 2025). However, data generated by bulk gas analysis of fluid inclusions have raised many theoretical and fundamental geochemical questions that, to our surprise, have not been addressed in the literature to date. The current study was inspired by a discussion between the authors and a colleague at the 2023 AGU Annual Meeting on whether the measured CO_2 from bulk gas analysis of inclusions represents $CO_{2\,(g)}$ and CO_{2aq} (as we assumed), or some or all of the Total Dissolved Inorganic Carbon (TDIC) in solution. Delving further into this topic, we found that even basic questions like "what happens to $CO_{2(aq)}$ and HCO_3^- when a solution is rapidly exposed to high vacuum?" have not been addressed. Answering this question is critical for determining whether CO_2 content measured on fluid inclusions truly represents the equilibrium between a brine and the overlying air during mineral formation. Other studies have recognized this problem (Hudgins et al., 2024; Park and Schaller, 2025), and Pettitt et al. (2020) assumed that the measured CO_2 from palustrine cherts from the Petrified Forest National Park (215 Ma) represents TDIC and not a mix between $CO_{2\,(g)}$ and $[CO_2]_{aq}$ (air and air-saturated brine CO_2). During analysis, inclusions hosted in minerals are mechanically decrepitated to release trapped volatiles into a high vacuum environment (10^{-7} to 10^{-8} mbar). Rapid exposure to pressures far below the vapor pressure of the liquid leads to fluid vaporization on millisecond timescales. Pettitt et al. (2020) assumed that the dissolved carbonate species (HCO_3^- and CO_3^{2-}) underwent protonation and dehydration reactions before exsolving into CO_2 gas during fluid vaporization. However, this assumption is unverified, and other studies hint that the majority of the HCO_3^- and CO_3^{2-} precipitate as a carbonate salt during rapid depressurization by combining with dissolved metal cations (Cui et al., 2001; McSween et al. 2003).

In this study, we test whether the CO_2 content measured from bulk gas analysis in fluid inclusions accurately represents the overlying air at various P_{CO2} levels during mineral formation, rather than the exsolution of some or all the TDIC. We hypothesize that the fluid inclusions in halite faithfully record the atmospheric conditions under which the mineral precipitated, and that the measured CO_2 content is derived solely from a mixture of CO_2 in air and $[CO_2]_{aq}$ from air-saturated brine. We predict that an insignificant amount of HCO_3^- and CO_3^{2-} will exsolve into CO_2, because as discussed in section 2, the carbonate reaction kinetics are too sluggish. To address this, we conducted depressurization experiments and bulk gas analysis via mass spectrometry on aqueous salt solutions equilibrated with air, and lab-grown halite that precipitated under controlled P_{CO2} atmospheres (450 ppm, 3000 ppm, and 5000 ppm).

2. Theoretical considerations

We can calculate how much $[HCO_3^-]$ and $[CO_3^{2-}]$ transform into CO_2 before inclusion fluid vaporization. If the measured CO_2 content represents the complete exsolution of TDIC, then previous studies have overestimated and misinterpreted their results.

The kinetics of the reactions within the carbonate (CO_2-H_2O) system is essential for understanding the above scenario and are controlled by the following reactions (Kern, 1960):

$$CO_{2\,(g)} \leftrightarrow [CO_2]_{(aq)} \qquad \text{(Eq. 1a)}$$

$$[CO_2]_{(aq)} + H_2O \leftrightarrow [H_2CO_3] \qquad \text{(Eq. 1b)}$$

$$[H_2CO_3] \leftrightarrow [H^+] + [HCO_3^-] \qquad \text{(Eq. 1c)}$$

$$[HCO_3^-] \leftrightarrow [H^+] + [CO_3^{2-}] \qquad \text{(Eq. 1d)}$$

$$[CO_2]_{(aq)} + H_2O \leftrightarrow [HCO_3^-] + [H^+] \qquad \text{(Eq. 1e)}$$

$$[CO_2]_{(aq)} + [OH^-] \leftrightarrow [HCO_3^-] \qquad \text{(Eq. 1f)}$$

In reaction (Eq. 1a), gaseous CO_2 is dissolved in water, and hydrolyzes to carbonic acid (Eq. 1b). Hydrogen ions dissociate from carbonic acid to form a bicarbonate ion (Eq. 1c), and further dissociation forms a carbonate ion (Eq. 1d).

The third reaction (Eq. 1c) is considered "instantaneous" (Kern, 1960), and it is impossible to determine whether the hydration reaction occurs directly through the second (Eq. 1b) and third (Eq. 1c) reaction or via the fifth reaction (Eq. 1e) (Eigen et al., 1961). The fifth reaction (Eq. 1e) is sluggish, making it the rate limiting reaction in low pH (<8.2) solutions; however, the sixth reaction (Eq. 1f) is favored at a high pH (>8.2) (Kern, 1960; Johnson, 1982; Dreybrodt et al., 1996). In table 1, k_{+1} to k_{+6} and k_{-1} to k_{-6} are, respectively, the forward and reverse reaction rate constants for the six reactions (Eq. 1a-f).

Assuming the reactions (Eq. 1a and e) are being driven to the left by depressurization, we can calculate the concentration of each species of interest (i.e., $[CO_2]_{aq}$ and $[HCO_3^-]$) that will exsolve before fluid vaporization under high vacuum (10^{-7} to 10^{-8} mbar). Based on our observations from the low-vacuum depressurization experiments in this study, complete fluid vaporization during decrepitation occurs within 5 milliseconds ($0.0004\ L \cdot s^{-1}$) (Data availability video). For the reverse reaction of Eq. 1a, the rate is given as:

$$-\frac{\partial [CO_2]_{aq}}{\partial t} = k_{-1} \cdot [CO_2]_{aq} \qquad \text{(Eq. 2a)}$$

Where $-\partial[CO_2]_{aq}/\partial t$ is the rate in $M \cdot s^{-1}$ and k_{-1} is the reverse kinetic rate constant for Eq. 1a (Table 1). Eq. 2a can be integrated to determine the $[CO_2]_{aq}$ at a given time:

$$[CO_2]_t = [CO_2]_0 \cdot e^{-k_{-1} \cdot t} \qquad \text{(Eq. 2b)}$$

Where $[CO_2]_t$ is the CO_2 concentration at a given time, $[CO_2]_0$ is the starting CO_2 concentration, and t is time in seconds. The rate for Eq. 1e is:

$$-\frac{\partial [HCO_3^-]}{\partial t} = k_{-5} \cdot [HCO_3^-] \cdot [H^+] \qquad \text{(Eq. 2c)}$$

Where $-\partial[HCO_3^-]/\partial t$ is the rate in $M \cdot s^{-1}$ and k_{-5} is the reverse kinetic rate constant for Eq. 1e (Table 1). Eq. 2c can be integrated to determine the $[HCO_3^-]$ at a given time:

$$[HCO_3^-]_t = [HCO_3^-]_0 \cdot e^{-k_{-5} \cdot [H^+] \cdot t} \qquad \text{(Eq. 2d)}$$

Where $[HCO_3^-]_t$ is the bicarbonate concentration at a given time and $[HCO_3^-]_0$ is the starting bicarbonate concentration. The exsolution of $[CO_3^{2-}]$ likely contributes a negligible amount to $[CO_2]_{aq}$ as $[CO_3^{2-}]$ requires protonation in two reaction steps (Eq. 1c and 1d) and is subsequently dehydrated (Eq. 1b). The exsolution of $[CO_3^{2-}]$ can be ignored as the time required for $[CO_3^{2-}]$ to exsolve into $[CO_2]_{aq}$ exceeds the inclusion fluid vaporization time (Kern, 1960). Pressure effects on the kinetics of the carbonate system are crucial to accurately characterize the depressurization of a carbonate solution during bulk gas analysis, yet they are poorly constrained. Eldik and Palmer (1982) and Millero and Berner (1972) suggest that changes in the carbonate system constants are negligible at low pressures (10^{-7} to 10^{-8} mbar). Pressure dependence has been investigated for reaction k_{-2}, showing a negative linear trend, with values indistinguishable between 1000 and 10,000 mbar (Eldik and Palmer, 1982). Moreover, Millero and Berner (1972) show that the carbonate equilibria constants do not change dramatically with decreasing pressure. Therefore, we assume the kinetic constants are similar to those at STP. Using Eq. 2d, we calculate that 0.0003% of the [HCO_3^-] would exsolve into [CO_2]$_{aq}$, after 5 milliseconds. Under these conditions, it would take 43 minutes for half of the [HCO_3^-] to exsolve into [CO_2]$_{aq}$. Furthermore, the reverse reaction of Eq. 1e is thermodynamically unfavorable, as the forward reaction is spontaneous (Kern 1960). Nonetheless, 0.004% of the [CO_2]$_{aq}$ would dissociate into [HCO_3^-]. Therefore, the kinetics of the carbonate system suggest that a negligible amount of [HCO_3^-] would be exsolved into [CO_2]$_{aq}$ during inclusion decrepitation. Reactions between metal cations and CO_2-H_2O system anions occurs more rapidly than the exsolution of [CO_2]$_{aq}$ because metal cations are electrostatically attracted to the carbonate species and complex easily with the negatively charged HCO_3^- and CO_3^{2-} in solution, promoting the rapid precipitation of carbonate salt after solution vaporization (Larson et al., 1973; Mullin, 2001; Henzler et al., 2018) (Appendix Fig. S1-2).

We can estimate how quickly $NaHCO_3$ precipitates during the decrepitation process by applying classical nucleation theory (Mullin, 2001), which is described as follows:

$$J = A\ exp\ (-\frac{1}{ln(\Omega)^2}) \qquad \text{(Eq. 3a)}$$

Where J is the rate of nucleation, A is the pre-exponential factor (or the frequency of molecular collisions), and Ω is the solution saturation index. In our context, the solution saturation can be written as:

$$\Omega = \frac{[Na^+][HCO_3^-]}{K_{sp\ (NaHCO3)}} \qquad \text{(Eq. 3b)}$$

Where $K_{sp\ (NaHCO3)}$ is the solubility constant for $NaHCO_3$ (Drever, 1997). A solution $\Omega > 1$ indicates that the solution is supersaturated with respect to the products. From Eq. 3a, the rate of nucleation is controlled by the degree of saturation. As saturation increases, the nucleation rate increases rapidly until $NaHCO_3$ salt precipitates. With the near instantaneous vaporization of the inclusion fluid, the solution becomes supersaturated almost instantaneously, causing the HCO_3^- and CO_3^{2-} to precipitate as a carbonate salt by combining with the dissolved metal cations. Given the rapid vaporization time compared to the slow reaction kinetics of the carbonate system, the exsolution of [HCO_3^-] and [CO_3^{2-}] would contribute a negligible amount to the measured CO_2 content.

3. Methods

3.1. Preparation of stock solutions

A 0.25 M $NaHCO_3$ solution and a 3.5 wt% Instant Ocean Sea Salt solution (spectrum brand) were made with Millipore water (18 MΩ·cm) and allowed to equilibrate with laboratory atmosphere. Solution pH, temperature, and overlying P_{CO2} were measured prior to experiments on an Oakton pH 150, a ThermoPro TP50 Digital hygrometer and thermometer, and an Aranet4 CO_2 meter, respectively. The Aranet4 CO_2 meter uses a nondispersive infrared sensor to measure the concentration of CO_2, and the reported error is the instrumental uncertainty associated with the individual measurements. The 3.5 wt% Instant Ocean Sea Salt solution was used to replicate modern ocean water conditions as it is an excellent comparison (Pretet et al., 2014). The carbonate species were calculated using the carbonate open system equations (Drever, 1997).

3.2. Low-vacuum depressurization experiments

To test whether rapid fluid vaporization of a carbonate solution leaves behind the expected mass of carbonate salt and to visually observe complete fluid vaporization, we performed depressurization experiments by placing 2 and 25 microliters of the 0.25 M $NaHCO_3$ solution inside a microcapsule using a syringe (Hamilton). The microcapsules were filled and placed in a glass vial connected to an ultratorr on a vacuum line, with temperature and pressure measured before the solution was exposed to a vacuum of 10^{-3} mbar (Fig. 1). The glass vial was exposed to vacuum until the solution in the microcapsule evaporated and the pressure stabilized. A video of the experiment being conducted in a capillary tube is available in the data availability section. After the vacuum experiment, the microcapsule was retrieved and weighed on a microbalance to determine the mass of the resulting $NaHCO_3$ salt. The 25 μL experiments were conducted in the same manner as the 2 μL experiments.

Gravimetric measurements of the stock solution in the microcapsule proved challenging because rapid evaporation of the small volumes of water prevented the microbalance from stabilizing, hindering accurate determinations of the amount of $NaHCO_3$ in individual experiments necessary for mass balance purposes. Instead, the average mass of the 2 μL and 25 μL stock solutions was determined gravimetrically by using the syringe to repeatedly decant the 2 μL and 25 μL solutions into an enclosed tin capsules to prevent evaporation; the mean of the 2 μL solution from the syringe was $\bar{x}$ =1.92 mg ($2\sigma = 0.23$; n = 25) and mean of the 25 μL was $\bar{x}$ = 25.19 ($2\sigma = 0.34$; n = 10).

3.3. Lab-grown halite crystals

Halite crystals were grown from NaCl (Fisher Science Education Brand: S25541) dissolved in Millipore water (18 MΩ·cm) under three experimental treatment conditions: one under normal laboratory P_{CO2} conditions and two under elevated P_{CO2} conditions (~3000 and ~5000 ppmV). Halite precipitated under open lab conditions formed under variable P_{CO2} of 774 ± 23 to 384 ± 12 ppm. This batch of halite precipitated under a temperature range of 23 ± 0.4°C to 26.7 ± 0.4°C, and P_{CO2} was monitored using an Aranet4 CO_2 meter. Additionally, halite crystals were grown under normal laboratory conditions with a 0.01 M $NaHCO_3$ solution added to the NaCl saturated water. Clean beakers and petri dishes were used to prevent biological material from altering the trapped gas chemistry. Halite precipitation at elevated P_{CO2} was achieved by placing NaCl saturated water into a sealed pressure vessel, which is designed to maintain unique atmospheric gas compositions (Fig. 1). The saturated halite solution was then placed inside the pressure vessel, sealed, and then purged with 'zero' grade dry air (Airgas) to remove the humidity and reduce the CO_2 concentration to near zero (Appendix Fig. S3). Following purging, 1000 mbar of zero grade air was injected into the pressure vessel to simulate the modern major atmospheric gas composition, as it is comparable (78.5 ± 2% N_2, 21.5 ± 2% O_2, balanced Ar; Airgas, Radon, PA, USA), minus humidity and CO_2. The CO_2 content was controlled by injecting medical grade CO_2 (Airgas) into the pressure vessel using a low-pressure regulator. CO_2 levels were monitored using the Aranet4 CO_2 meter placed inside the pressure vessel (Fig. 1). Two batches of halite crystals were precipitated under two elevated P_{CO2} conditions.

The first batch of halite grown at elevated P_{CO2} precipitated over the course of a few days, during which P_{CO2} increased from an initial minimum of 3020 ± 91 ppm to a final maximum of 3568 ± 107 ppm, with temperatures ranging from 17.6 ± 0.4°C to 20.1 ± 0.4°C. The second batch precipitated under similar conditions, with P_{CO2} increasing from an initial minimum of 4705 ± 141 ppm to a final maximum of 5329 ± 160 ppm, and temperatures ranging from 18.5 ± 0.4 to 20.6 ± 0.4°C. During halite precipitation, pressure and humidity were also monitored using the Aranet4 CO_2 meter (Appendix Fig. S4). In the halite samples, gas solubility is primarily influenced by sodium and chlorine ions. Although, other cations and anions are likely present, their impact on gas solubility is considered negligible and therefore excluded (Hermann et al., 1995). The precipitated halite contains both primary aqueous and gaseous fluid inclusions.

3.4. Measuring volatile contents from fluid inclusions in halite and stock solutions by mass spectrometry

Following the methods of Pettitt and Schaller (2020) and Park and Schaller (2025), 60 to 120 milligrams of lab-grown halite was loaded into a custom inlet, and mechanically decrepitated to release the trapped gaseous and aqueous volatiles directly into a Pfeiffer Prisma Plus 1-100 amu quadrupole mass spectrometer (QMS). Adsorbed gases were removed from the samples by pumping them to a high vacuum (10^{-7} to 10^{-8} mbar). 0.2 microliters of 3.5 wt% Instant Ocean salt and 0.25 M $NaHCO_3$ solutions were loaded into a calibrated pipet volume using a syringe (Hamilton). The solution volume fully occupied the pipet to achieve a minimal amount of headspace. To isolate the solutions from the high vacuum inlet, a cobalt alloy ball stem tip (Swagelok) is compressed onto the mating surface of the volume pipet, forming a gas-tight seal (Pettitt and Schaller, 2020) (Fig. 1). Solutions encapsulated in the pipettes were loaded into the custom inlet, evacuated to high vacuum, and rapidly depressurized, releasing the volatiles through a water trap and directly into the QMS. Similarly, halite samples were crushed into the inlet and the gases were directed through the water trap into the QMS. Upon introduction to the QMS, volatiles produce transient peaks in ion current on a secondary electron multiplier. The quadrupole is tuned to monitor the ion current at m/z 14, 15, 16, 18, 28, 32, 40, and 44 with a 50 millisecond dwell time at each nominal mass. M/z 14 is used to quantify N_2^+ due to a mass interference from CO^+ at m/z 28 (Graney and Kesler, 1995; Pettitt and Schaller, 2020). Although, CH_4^+ contributes to m/z 14, its signal is corrected using a separate methane calibration based on calculating the fragmentation from m/z 15 and 16. H_2O^+, O_2^+, Ar^+, and CO_2^+ were measured at m/z 18, 32, 40, and 44, respectively. A cold cathode ion gauge was used jointly with the QMS, and a rise in pressure is observed along with the peaks in ion current. The pressure change is used as a metric for total gas released from each crush. Pettitt and Schaller (2020) show that there is no observable effect of the cold cathode gauge on the measured gas composition as the gauge is active during both calibration and sample analyses.

The integrated area of the ion current peak for each species is compared to a calibration curve generated from a calibrated gas mixture and used to quantify the total moles of each gas in the unknown samples. For more details about the instrument setup, calibration method, and measured gas composition errors and reproducibility, consult Pettit and Schaller (2020), Pettitt et al. (2020), and Park and Schaller (2025). Calibration is performed by filling pipette volumes with a dry air standard (78.18±1.56% N_2, 20.84±0.42% O_2, 0.938±0.019% Ar, and 391.1±7.8 ppm CO_2; Airgas, Radnor, PA, USA) at controlled pressures and temperatures, and then releasing the gas into the instrument for quantification (Pettitt and Schaller, 2020). This calibration method simulates the pulsed release of gases during crushing and enables quantification down to the femtomol level.

3.5. Gas-aqueous partitioning of volatiles

The gas phase in the experimental stock solutions (if present) corresponds to the headspace when the stainless steel volume pipet is sealed off with the stem tip (Fig. 1C-1), whereas the aqueous phase is comprised of the dissolved atmospheric gases at equilibrium with the atmosphere at the time of isolation. For inclusions in the lab-grown halite, the gas phase corresponds to the atmosphere under which the halite precipitated, whereas the aqueous phase are the atmospheric gases dissolved at equilibrium. Because of the multiphase nature of these experiments, the composition of the released gases are expected to fall along a spectrum between the fully gaseous and fully aqueous end-members. Thus, the gas and aqueous composition must be partitioned to determine the true composition of the atmosphere under which the stock solution and lab-grown halite equilibrated. This gas-aqueous partitioning procedure (MAGPI: Method for Atmospheric Gas Partitioning from fluid Inclusions) is briefly described below, but consult Park and Schaller (2025) for details on the method development and source code. The gas-aqueous partitioning method relies on the following assumptions: (1) the volatiles trapped within the fluid inclusions were in equilibrium with the overlying atmosphere at the time of entrapment; (2) the trapped volatiles have retained their original composition, with no addition or loss of volatiles due to radioactive decay of e.g., ^{40}K, diffusion, dissolution, or biologic processes since fluid inclusion closure; and (3) the original formation temperature and salinity has not been altered after closure. Formation temperature and salinity can be independently constrained using micro-thermometry and Raman spectroscopy (Guillerm et al., 2025; Sun et al., 2010; Wang et al., 2018). Partitioning the gas phase from the aqueous phase is based on the measured gas ratios (e.g., N_2/Ar). The gas ratios can be used to partition the contributions from both the gaseous and aqueous phases to obtain the true atmospheric composition by using:

$$X_j^{atm} = \frac{n_j^{obs}}{\left(\frac{\varphi_g}{RT}+(1-\varphi_g)H_s^i(T,S)\right)}\left[\sum_{i=1}^{M}\frac{n_i^{obs}}{\left(\frac{\varphi_g}{RT}+(1-\varphi_g)H_s^i(T,S)\right)}\right]^{-1} \qquad \text{(Eq. 4)}$$

Where X_j^{atm} is the mole fraction of the atmospheric component of volatile j, defined as the number of moles of the volatile of interest normalized to the summation of the total moles released during the experiment (N_2, O_2, Ar, and CO_2); n_j^{obs} is the moles observed of the volatile of interest; M are the volatiles taken into consideration (N_2, O_2, Ar, and CO_2); n_i^{obs} is the moles of gas i observed in the analysis (gas + aqueous); φ_g is the gas volume fraction calculated from the N_2/Ar ratio; R is the universal gas constant; T is the temperature of the fluid inclusion in Kelvin; H_S^i is the temperature and salinity dependent Henry's solubility constant ($mol \cdot L^{-1} \cdot atm^{-1}$) of the gas of interest; and S is the salinity of the fluid inclusion. The solubility of each gas is dependent on the temperature and the salinity of the brine (Onda et al., 1970; Hermann et al., 1995). MAGPI was used to perform the calculations on all the decrepitation and depressurization data present in this study. Our measured gas contents are reported with uncertainties at the 95% confidence interval. Errors are propagated using standard techniques following Ku (1996).

3.6. Raman spectroscopy

Raman spectroscopy is employed to meet several objectives: 1. To test whether the residue from the low-vacuum depressurization experiment is $NaHCO_3$ salt; 2. To determine inclusion salinity so that an accurate Henry's solubility constant is used for calculating the gas volume fraction; and 3. To further validate that the fluid inclusions in lab-grown halite capture the overlying atmosphere during precipitation by analyzing gas dominated inclusions. Salinity calibration and inclusion analysis were performed on a Horiba XploRA confocal Raman spectrometer at Rensselaer Polytechnic Institute (RPI) following the calibration technique of Sun et al. (2010), described below. Analysis of the experimental residue was performed on a Bruker

Senterra Raman spectrometer at RPI. Measurements on both instruments use a 532 nm green laser at 20 mW power. Using a 600-diffraction grating, measurements were made with a 50x objective and a 50 µm aperture at 2 cm^{-1} spectral resolution. Experiments were integrated for 30 seconds with 3 accumulations. Analysis of the gas dominated inclusion used a 1200-diffraction grating and was integrated for 300 seconds with 3 accumulations. Raman spectra were exported to OriginPro graphing and analysis software and background corrected.

We performed laser Raman spectroscopy on the low-vacuum experimental residue to determine whether the residue is in fact $NaHCO_3$ salt in either the amorphous or the expected crystalline form. $NaHCO_3$ has four main Raman active bands, where weak bands occur at 688 cm^{-1} (ν_4, in-plane deformation) and 1432 cm^{-1} (ν_3, C–O antisymmetric stretch), a medium strength band at 1271 cm^{-1} (ν_1, C–O symmetric stretch), a very strong band at 1048 cm^{-1} (ν_1, C–O symmetric stretch), and eight translational lattice bands between 80-250 cm^{-1} (Frezzotti et al., 2012). We compared the spectra of the experimental residue to the original $NaHCO_3$ salt as well as to the glass microcapsule.

Accurate temperature and salinity data are essential for calculating Henry's solubility constants for each volatile species (N_2, O_2, Ar, and CO_2), and are necessary inputs to the gas-aqueous partitioning calculation using MAGPI (Park and Schaller, 2025). The temperatures of the stock solutions were recorded prior to loading onto the high-vacuum inlet for gas analysis, whereas the temperature used for corrections on the lab-grown halite corresponds to the formation temperature at which the halite precipitated inside the sealed pressure vessel. Stock solution salinity was determined from the added constituents. The salinity of the fluid inclusions in halite was quantified using Raman spectroscopy following the method of Sun et al. (2010), by constructing an in-house calibration curve to determine [Cl^-] in the inclusions, which were then converted to an equivalent NaCl salinities. Salinity of the NaCl solution was determined via Raman spectroscopy rather than relying on the initial aqueous concentrations because evaporation during halite precipitation increases brine salinity to an unknown value (Lowenstein et al., 2001). The salinity of the trapped brine in the inclusion is the salinity of the brine at the time of precipitation, and determination via Raman spectroscopy is a reliable and accurate method to quantify inclusion salinity in the lab-grown halite (He et al., 2024; Sun, 2009; Sun et al., 2010). [Cl^-] was estimated based on the relative intensity changes of the two deconvoluted peaks at 3220 cm^{-1} and at 3450 cm^{-1} in the OH^- stretch for H_2O, relative to the corresponding peaks for pure H_2O. Deconvolution was performed in the OriginPro graphing and analysis software. The average salinity of the lab-grown halite is ~39 wt% (~6.7 mol/L of NaCl) (Appendix Fig. S5).

Validation was accomplished by in-situ laser Raman spectroscopic analysis of a gas-dominated fluid inclusion, which demonstrates that fluid inclusions in halite trap samples of atmospheric gases during mineral formation. This was accomplished by comparing the atmospheric N_2/O_2 ratio under which the lab-grown halite precipitated to the N_2/O_2 intensity ratio of the gas trapped within the inclusion. The similar Raman cross-sections between N_2 and O_2 allow their Raman intensities to facilitate direct comparisons between N_2 and O_2 trapped within the inclusion (Fouche and Chang, 1971; Fenner et al., 1973). N_2 has one strong Raman active band at 2331 cm^{-1} (N≡N stretch) and O_2 has one strong Raman active band at 1555 cm^{-1} (O=O stretch) (Burke, 2001; Frezzotti et al., 2012). Further comparisons were made between the measured N_2/O_2 values from the bulk gas analyses and the N_2/O_2 intensity ratios obtained by the Raman spectrometer. Both the Raman spectra and the gas analyses are expected to reflect the

N_2/O_2 ratio under which the lab-grown halite precipitated (3.73 ± 0.2), a value similar to the modern atmosphere (Brimblecombe, 1996). Because halite is isotropic, and therefore does not have birefringence, the halite mineralogy will not affect the quantification and the Raman peak intensities of N_2 and O_2 (Caumon et al., 2015). Furthermore, a confocal Raman spectrometer was used, which bypasses the halite crystal ensuring that is does not contribute to the analysis (Fries and Steele, 2011).

4. Results

4.1. Low-vacuum depressurization experiments of a carbonate solution

Masses of the residues resulting from the low-vacuum depressurization experiments fall on the 1:1 line for both the 2 μL ($\bar{x} = 0.043$ mg; $\sigma = 0.003$; $n = 10$) and 25 μL ($\bar{x} = 0.523$ mg; $\sigma = 0.009$; $n = 2$) volumes, and are within the expected syringe-mass procedural error (2 μL; 0.043 mg ± 0.003, and 25 μL; 0.525 mg ± 0.014) (Fig. 2 and Table 2). Our experimental results do not noticeably deviate from the expected yields based on calculations in section 3.2, suggesting that the majority of HCO_3^- and CO_3^{2-} does not transform into CO_2. Although, the amount of CO_2 released could not be quantified as the equipment used did not have enough significant figures to accurately quantify the expected CO_2 loss gravimetrically, CO_2 was quantified during the depressurization and decrepitation experiments performed on the QMS.

Peaks in the Raman spectra of the experimental residue match those in the spectrum of the original $NaHCO_3$ salt (Fig. 3), confirming that the residue is the original carbonate salt (and is distinct from glass microcapsule). The main Raman bands are observed at 688 cm^{-1}, 1048 cm^{-1}, and 1271 cm^{-1}, matching those of $NaHCO_3$ (Frezzotti et al., 2012). Additional Raman bands occur at 1017 cm^{-1} and 1064 cm^{-1} corresponding to HCO_3^- and CO_3^{2-}, respectively (Davis and Oliver, 1972). However, the weaker HCO_3^- band at 1360 cm^{-1} is not present within the residue spectra (Frezzotti et al., 2012), which is likely obscured due to a fluorescence effect from the Raman spectrometer. The residue's translational lattice band structure is consistent with that of $NaHCO_3$, indicating that the residue is crystalline. However, the broadening of the spectral bands at 1048 cm^{-1} and within the translational lattice range at 228 cm^{-1}, 205 cm^{-1}, 166 cm^{-1}, 153 cm^{-1}, 145 cm^{-1}, 114 cm^{-1}, and 92 cm^{-1} suggest that some of the residue is amorphous. A partly amorphous structure of the experimental residue is likely a consequence of rapid $NaHCO_3$ precipitation during solution vaporization, and therefore consistent with our initial hypothesis.

4.2. Quadrupole mass spectrometry depressurization and decrepitation experiments

Quadrupole mass spectrometry was used to quantify the abundance of the major atmospheric gases in the stock solutions and lab-grown halite. We observe mole fractions that lie between the air and air-saturated brine (ASB) endmembers with varied gas volume fractions (Appendix Fig. S***6***). The measured CO_2 mol percent (mol%) and CO_2 normalized to argon (CO_2/Ar) were both compared to expected values calculated using the partial pressure and aqueous solubility of each gas, the gas volume fraction (φ_g), and the temperature and salinity of the solution. φ_g was obtained from the measured N_2/Ar ratios. Assuming that the gas content solely originates from an air-ASB mixture, the expected molar abundance of each gas of interest is calculated using the following equation:

$$n_j^{calc} = P_i V \left[\frac{\varphi_g}{RT} + (1 - \varphi_g) H_s^i(T, S)\right] \qquad \text{(Eq. 5)}$$

Where n_j^{calc} is the number of mols for each gas of interest; P_i is the partial pressure of the gas of interest where P_{N2}, P_{O2}, P_{Ar} was set to 0.7808, 0.2095, and 0.093, while P_{CO2} was adjusted to the measured P_{CO2} values from the Aranet4. Solubility constants were adjusted to the measured temperature and salinity values. From the calculated expected molar abundance, an expected CO_2 mol% and CO_2/Ar for a given gas volume fraction can be estimated, allowing for comparisons with the measured CO_2 content. The measured vs expected CO_2% and CO_2/Ar show a linear relationship that closely aligns with the 1:1 slope corresponding to CO_2 derived solely from an air-ASB mixture (Fig. 4 and consult Table 3 for regression equations). We statistically evaluate whether the measured versus expected averages and slopes deviate from the 1:1 using both analysis of variance (ANOVA) and analysis of covariance (ANCOVA) tests. ANOVA compares the averages of two or more groups by analyzing variance, while ANCOVA compares the regression slopes of two or more groups by analyzing the means of the dependent variable (McDonald, 2014). The ANOVA test of the measured CO_2% and CO_2/Ar are statistically indistinguishable from the 1:1 line (Fig. 4 and consult Table 3 for statistics). The ANCOVA test of the measured CO_2% and CO_2/Ar slopes show statistically significant deviation from the slope of the 1:1 line. This deviation may be due to the argon normalization and mol% slightly shifting the slope from the 1:1 line. However, the homogeneity of regression slopes between the measured CO_2% and CO_2/Ar and the 1:1 line are statistically parallel to one another.

Using equation 4, a unique correction was applied to each of the stock solutions and lab-grown halite analyses (Park and Schaller, 2025). The raw data was partitioned into their gaseous and aqueous endmembers to determine the atmospheric composition that each equilibrated with. When partitioned, the N_2, O_2, and Ar accurately reflect the modern atmosphere and the atmosphere used inside the pressure vessel (Appendix Fig. S7). The partitioned CO_2 from the lab-grown halite that precipitated under "normal" and elevated P_{CO2} fall within the expected P_{CO2} range of their respective conditions (Fig. 5 and Table 4). Because laboratory P_{CO2} is variable, the P_{CO2} with which the stock solutions had equilibrated was recorded before the setup of each depressurization experiment. The partitioned CO_2 from the stock solutions falls along the expected 1:1 line corresponding to P_{CO2} measured by the Aranet4. CO_2% and CO_2/Ar of the unpartitioned and partitioned gases from the stock solutions and lab-grown halite are compared to each other and shown in Fig. 6 and values are in Table 5.

4.3. Depressurization and total dissolved inorganic carbon

To test whether the measured CO_2 solely represents air-ASB CO_2 or the exsolution of TDIC, we modeled the expected CO_2 content for both end-member scenarios over a range of gas volume fractions (φ_g). The modeled CO_2% and CO_2/Ar for an air-ASB mixture were calculated using equation 5. In contrast, the complete TDIC exsolution model was generated by estimating TDIC from the measured pH, P_{CO2}, temperature, and salinity of each solution, using the open carbonate system equations (Drever, 1997). For this model, we assumed that the TDIC completely exsolved into $CO_{2\,(aq)}$, and the resulting $CO_{2\,(aq)}$ was used with the appropriate Henry's constant in equation 5. The solubility constants were adjusted to the measured temperature, salinity, and whether the solution was NaCl or $NaHCO_3$ dominated, producing a unique CO_2 model for each stock solution (Hermann et al., 1995). We then compared the measured CO_2 content from each stock solution to the modeled expectation as a function of φ_g (Fig. 7). The measured CO_2% (<1%) and CO_2/Ar (<1) values are consistent with the air-ASB CO_2 model at the measured gas volume fraction range (0.01-0.12). In contrast, the complete exsolution of TDIC model yields CO_2 75 ± 15% and 500 ± 354 CO_2/Ar for the same gas volume fraction range (Fig. 7). TDIC exsolution models were not calculated for the lab-grown halite, as the inclusion pH could not be estimated. Although we attempted to quantify inclusion pH using the Raman method of Hudgins et al. (2024), it was unsuccessful at these concentrations. However, if we assume that the initial pH of the halite solution reflects the inclusion pH, the measured lab-grown halite CO_2 content aligns with the air-ASB CO_2 model for a given φ_g (Appendix Fig. S8).

4.4. Raman spectra of a gas dominated lab-grown inclusion

Raman analysis on a gas dominated inclusion shows the main peaks for N_2 and O_2 present at 2331 cm^{-1} and 1555 cm^{-1} (Burke, 2001; Frezzotti et al., 2012) (Fig. 8). Ratioed peak intensities of N_2 and O_2 (I_{N2}/I_{O2}) give a value of 3.84 ± 0.2, which closely aligns with the atmospheric value under which the halite precipitated (3.73 ± 0.2), and is distinct from the aqueous end-member ratio of 1.73 ± 0.2. Furthermore, the I_{N2}/I_{O2} is in range with the partitioned N_2/O_2 contents of the lab-grown halite and stock solutions bulk gas analyses ($\bar{x} = 3.78 \pm 0.24$) (Fig. 9). This suggests that direct N_2/O_2 measurements can be obtained prior to the ice core record via Raman spectroscopic methods (Ikeda et al., 1999; Ohno et al., 2021). Future hypothesis testing should focus on measuring N_2/O_2 in natural samples, and testing whether N_2 or O_2 is excluded during halite crystallization, similar to the ice core record (Severinghaus and Battle, 2006). However, in our analysis, it does not appear that the lab-grown halite preferentially incorporates any one gas during crystallization.

5. Discussion

5.1. CO_2 from inclusion analysis is a mix of air and air-saturated brine

The measured CO_2 from the depressurization and decrepitation experiments are in close agreement with the expected endmembers of air-ASB, and not the complete or even partial exsolution of TDIC (Fig. 4, 6, 7). This observation is supported by the statistically identical averages and the significant homogeneity of regression of the expected versus measured CO_2 (Fig. 4 and Table 3), and the large differences between the measured CO_2 content and the complete TDIC exsolution model (Fig. 7). Our data are also consistent with the kinetics of the carbonate system equilibria, showing that equilibrium is too sluggish to allow exsolution of a substantial amount of HCO_3^- or CO_3^{2-} during fluid inclusion decrepitation. During fluid vaporization, the solution is supersaturated with respect to $NaHCO_3$, causing rapid nucleation of carbonate salts (Mullin, 2001). Therefore, a carbonate salt residue should be observed after both the low-vacuum and QMS depressurization experiments. As shown in section 4.1, the white residue remaining in the microcapsule following the low-vacuum experiments has a Raman spectrum consistent with $NaHCO_3$ salt, and the mass of the precipitate confirms that a quantitative conversion occurred (Fig. 2 and 3). The mass of the residue around the rim of the volume pipets following the QMS depressurization experiment was not collected because the volume pipet greatly exceeds the mass limitation of the RPI microbalance (Mettler Toledo XP6). Carbonate salt precipitation following boil off of the solution water is supported by experiments on 1 wt% Na_2CO_3 and $NaHCO_3$ solutions (Cui et al., 2001). However, Cui et al. (2001) did not measure the mass of the residue to confirm a quantitative conversion had occurred, and these experiments were conducted at ca. 1 atm, not under vacuum.

In the short time between rupturing a fluid inclusion, but before fluid vaporization, partial exsolution of TDIC could occur in principle, and could contribute to the measured CO_2 content, potentially inflating measured CO_2 values. To explore this possibility, we theoretically estimate the magnitude of this contribution to the measured CO_2 content. Over the 5 milliseconds to boil off the inclusion fluid during decrepitation, 0.0003% of the [HCO_3^-] would be converted to [CO_2]$_{aq}$ via the reverse reaction of Eq. 1e (Kern, 1960). Although, the reverse reaction of Eq. 1e is thermodynamically unfavorable under natural water conditions (Drever, 1997), 0.004% of [CO_2]$_{aq}$ would contribute to [HCO_3^-] via the forward reaction. These contributions are exceedingly small compared to the relative error of the CO_2 measurements in our analysis, which was determined from the 95% confidence intervals ($\bar{x} = 6.4\%$; $\sigma = 5.1\%$). Therefore, the potential contribution of partial TDIC exsolution to the measured CO_2 content is indistinguishable from the instrument uncertainty and does not merit correction.

Uncertainty on the measured CO_2 content and minor deviations from the 1:1 line (Fig. 4) cannot be explained by partial DIC exsolution but may be due to limitations of the analytical technique. The CO_2 content is often quantified close to its femtomol limit of detection, which may account for some of the variation between the expected versus measured (Pettitt and Schaller, 2020). Furthermore, the effects of solubility are the greatest for CO_2, as its high solubility results in the most significant compositional differences between the gaseous and aqueous phases. Uncertainty in φ_g will disproportionately affect CO_2 relative to the other gases (Park and Schaller, 2025). Another contributing factor to the error and deviation of CO_2 is likely the variability of the P_{CO2} levels measured by the Aranet4, as the associated error of the P_{CO2} increases with higher partial pressure (0-2000 ppm ± 3% and 2001-9999 ± 10%).

Prior to gas-aqueous partitioning, the measured CO_2 content of the lab-grown halite and stock solutions fall between the expected endmembers of an air-ASB mixture (Fig. 4). However, because CO_2 is highly soluble, interpreting unpartitioned CO_2 from multiphase inclusions as the atmospheric condition will lead to erroneous conclusions. For example, the unpartitioned CO_2 content of halite grown at ~3000 ppm could be interpreted as having an average P_{CO2} of 112,851 ± 61,200 ppm (Table 4). In contrast, partitioning the same data yields an average P_{CO2} of 2918 ± 263 ppm, which closely matches the measured P_{CO2} the halite precipitated under (Fig. 5 and Table 4). This trend is consistent in the measured CO_2 content, as well as the other gaseous species, in the lab-grown halite and stock solutions (Fig. 5 and 6, Table 4, and Appendix Fig. S7). These findings reinforce that gas-aqueous partitioning is an essential step in inclusion gas analyses to accurately reconstruct atmospheric conditions.

5.2. Biological influences on fluid inclusions in halite

The variability within our data could also be caused by biological processes (e.g., photosynthesis and respiration) altering the O_2 and CO_2 gas chemistry of the fluids trapped within the inclusions, resulting in a gas composition that departs from the expected atmospheric conditions. Although this is a far greater concern on natural samples as complex organic molecules and living microorganisms have been observed in fluid inclusions (Vreeland et al., 2000; Mißbach et al., 2021; Schreder-Gomes et al., 2022; Gibson and Benison, 2023), it is possible that microorganisms and organic matter could have been trapped in fluid inclusions during precipitation of the lab-grown halite, altering the gas chemistry. Despite methodological efforts to avoid this, Raman spectroscopy can verify the presence or absence of trapped organic matter or microorganisms. Raman spectra of fluid inclusions from the lab-grown halite do not show peaks associated with organic molecules (Appendix Fig. S9) (Fries and Steele, 2011; Lu et al., 2011). However, it is possible that organic matter or microbes were not detected by the Raman spectrometer if the analyte of interest was below the limit of detection. An additional test to determine biological influence on the lab-grown halite data follows the method of Park and

Schaller (2025). To determine if the O_2 and CO_2 measured is influenced by the expected stoichiometric exchange due to photosynthesis or respiration, the expected molar abundance of each gas is calculated relative to the observed moles of N_2 and compared to what is observed. The difference between the observed and expected moles of the two gases can be calculated through the gas-aqueous partition:

$$\Delta n_j = n_j^{obs} - \left(\frac{X_j^{atm}}{X_{N_2}^{atm}} * n_{N_2}^{obs} \frac{\left(\frac{\varphi g}{RT} + (1-\varphi_g) H_s(T,S)\right)_j}{\left(\frac{\varphi g}{RT} + (1-\varphi_g) H_s(T,S)\right)_{N_2}} \right) \qquad \text{(eq. 6)}$$

Where j is the gas of interest, the X_j/X_{N2} term is set to reflect the ratios of the modern atmosphere. Excesses and deficits of O_2 and CO_2 can be compared by plotting the ΔO_2 and ΔCO_2. If photosynthesis or respiration has modified the inclusion gases, then a 1:1 inverse relationship between the gases should be observed. Although the stoichiometric relationship between photosynthesis and respiration can vary depending on other factors such as the oxidation state of carbon (Smart et al., 2025), these considerations are beyond the scope of this paper and a 1:1 stoichiometric relationship is assumed for the laboratory grown samples. The deficits and excesses in CO_2 and O_2 do not exhibit clear trends indicative to photosynthesis or respiration (Fig. 10). Although, the causes of the deficits and excesses remain unclear, partitioning the gas data accurately reflects the expected atmospheric conditions under which the mineral precipitated and stock solutions equilibrated (Fig. 5, 6, and 9). The larger deficits and excesses observed in the stock solutions relative to the lab-grown halite are due to the physically larger sample volume.

5.3. Inclusions in halite capture a 'snapshot' of the atmosphere

By analyzing air bubbles trapped in glacial ice, the Antarctic ice core record has provided direct compositional measurements of the atmosphere of the last 800 Ka with some isolated intervals dating back to 2 million years (Lüthi et al., 2008; Higgins et al., 2015; Yan et al., 2019). Prior to the ice core record, reconstructing Earth's ancient atmospheric composition has relied on models and a variety of proxy methods that in some time periods disagree in overall trends and absolute values for P_{CO2} (CenCO2PIP, 2023). However, as shown by this study and Park and Schaller (2025), inclusions in lab-grown halite clearly trap atmospheric gases during mineral precipitation, where the halite precipitated under controlled atmospheric conditions align with gas compositions introduced into the growth chamber (Fig. 5) (Appendix Fig. S7). Although, Park and Schaller (2025) grew halite in laboratory conditions, this study better controlled the atmospheric conditions during halite precipitation using a sealed pressure vessel and at elevated P_{CO2}. Notably, the halite that precipitated under different CO_2 atmospheres yields measured CO_2 compositions that, when partitioned, correspond to the respective CO_2 conditions under which the halite precipitated. In addition, Raman spectra of a gas dominated inclusion provides secondary evidence that the inclusions in halite trap the atmosphere during mineral formation and are further corroborated with the partitioned N_2/O_2 gas data (Fig. 8 and 9).

Bulk gas analyses of inclusions trapped in halite have the potential to extend direct atmospheric compositional (and isotopic) constraints beyond the ice core record (Goldstein, 2001), as this study further confirms that CO_2 and O_2 can be directly quantified and partitioned to reflect the true atmosphere during halite formation (Park and Schaller, 2025) (Appendix Fig. S7). This approach can be used to test Earth's degassing history (e.g., Baekert et al 2025), as well as the evolution and interplay between the atmosphere, biosphere, lithosphere, and hydrosphere.

Specifically, this approach can test whether continental weathering can be the main control of long term P_{CO2} levels (Kent and Muttoni, 2013; Schaller et al., 2015), the relationship between the global mean temperature and increasing P_{CO2} (Caballero and Huber, 2013), and whether the $\delta^{13}C$ of mantle derived CO_2 has been consistent or varied throughout Earth history (Des Marais and Moore, 1984; Krissansen-Totton et al., 2021). For example, Park et al. (2025) report a $\delta^{13}C$ value of -8.38 ± 0.20 ‰ (VPDB) for CO_2 trapped in halite inclusions from the Mesoproterozoic Sibley halite (Ontario, Canada), a value that supports a relatively consistent atmospheric $\delta^{13}C$ through the last 1.4 Ga. Further, after applying the appropriate carbon isotope fractionations during gas-water exchange, this value predicts calcite formation with $\delta^{13}C$ between -0.2 ‰ and 1.6 ‰ (VPDB at 10-30°C, respectively), which matches the value of contemporaneous 1.4 Ga marine carbonates (Krissansen-Totton et al., 2015). This approach outlines how bulk gas analysis of inclusions in halite have the potential to address unresolved questions that are crucial for quantitative long-term global carbon cycle models and future CO_2 projections (Berner et al., 1983; Foster et al., 2017).

Extending the record of Earth's atmospheric CO_2 content beyond the ice cores has heretofore relied on proxies, where the physical, biological, or geochemical property of a fossil or mineral responds to or records some function of the concentration of CO_2 during formation (Royer, 2014). However, inclusions in halite have the potential to extend the direct CO_2 record beyond the temporally restricted ice cores (Yan et al., 2019), as we have shown that halite trap gases that are representative of the overlying atmosphere under which they precipitated. Furthermore, the low diffusivity of H_2 and CO_2 through halite at temperatures below 200°C indicates atmospheric gases can be retained within the mineral for billions of years (Zimmermann and Moretto, 1996). Although, post-depositional processes will alter the initial inclusion chemistry, robust screening protocols are used to identify and exclude altered samples, such as, petrography, micro-thermometry, and Raman spectroscopy. See Blamey and Brand (2019), and Brand et al. (2021) for a detailed review of the screening protocol for primary inclusions in halite. Moreover, bulk gas analysis of inclusions is not limited to halite samples as palustrine cherts, soil carbonates, and soil gypsum have produced mole fractions of atmospheric gas compositions that are in excellent agreement with previous model predictions (Pettitt et al., 2020).

6. Conclusions

We test whether the CO_2 content measured from bulk gas analysis in fluid inclusions accurately represents the overlying air at various P_{CO2} levels during mineral formation, rather than Pettitt et al's. (2020) assumption that the CO_2 measured represents the complete exsolution of TDIC. We find Pettitt et al's. (2020) assumption to be unsupported. We demonstrate that the CO_2 contents measured in inclusions hosted in halite accurately represents the overlying air at various P_{CO2} levels, rather than the complete or partial exsolution of TDIC. Our results show that the measured CO_2 content falls between the expected values of air and air-saturated brine at different CO_2 conditions, and by partitioning gas contributions from each phase, we observe atmospheric P_{CO2} values closely matching the conditions under which the lab-grown halite precipitated. These findings demonstrate the ability of halite inclusions to faithfully entrap and preserve atmospheric CO_2 but also the other major atmospheric gases (i.e., N_2, O_2, and Ar), giving us confidence in applying our methods to new and existing analyses of both natural modern and ancient halite-inclusions. Future work should conduct bulk gas analysis on fluid inclusions in halite that are grown at elevated temperatures (100-200°C) and synthesized from natural seawater or other natural brines to constrain physical and biological alteration pathways. Bulk inclusion gas analysis should be extended to other minerals, such as soil carbonates, soil gypsum, and cherts. Bulk gas analysis of fluid inclusions is a promising method to reliably reconstruct the atmospheric composition beyond the ice core record.

CRediT Authorship Contribution Statement

Michael Naylor Hudgins: Conceptualization, Methodology, Formal Analysis, Investigation, Data Curation, Writing – Original Draft, Visualization. **Justin G. Park:** Investigation, Writing – Review & Editing. **Alex M. Ryan:** Investigation, Writing – Review & Editing. **Jessika Rogers:** Investigation, Writing – Review & Editing. **Morgan F. Schaller:** Conceptualization, Resources, Writing – Review & Editing, Supervision.

Data Availability

All data necessary to evaluate the conclusions of this study are available through Mendeley Data at https://data.mendeley.com/datasets/jzcbs7fjnx/1**.**

Declaration of Competing Interest

The authors declare that they have no known competing financial interests or personal relationships that could have appeared to influence the work reported in this paper.

Acknowledgements

A special thank you to Andy Ridgwell, who brought this criticism to our attention following our presentation at the 2023 AGU meeting, as well as many fruitful discussions with Wally Broecker. Thank you to Neha Dhull, Matthew Pasek, Frank Spear, and Sasha Wagner for enlightening discussions and to Humberto Terrones for the use of the Raman spectrometer. We are grateful for the support and help from the CESIA and RARE members. We thank Sean T. Brennan, Daniel Breecker, and one anonymous reviewer for their comments and suggestions that greatly improved this manuscript.

Appendix A. Supplementary Material

The supplement contains a video of the low-depressurization experiment; thermodynamic and classical nucleation theory; figures of the theoretical calculations; figures including Aranet4 CO_2 meter calibrations and other monitored parameters (temperature, relative humidity, and pressure); Raman spectra used to estimate fluid inclusion salinity and to qualitatively identify organic matter; measurements of other major gases (N_2, O_2, and Ar) from the bulk gas analysis; and additional CO_2 models that support the study's conclusions. The Supplementary Material to this article can be found online at DOI: ###.

References

Berner R. A., Lasaga A. C. and Garrels R. M. (1983) The carbonate-silicate geochemical cycle and its effect on atmospheric carbon dioxide over the past 100 million years. *Am. J. Sci.* 283, 641–683.

Blamey N. J. F. and Brand U. (2019) Atmospheric gas in modern and ancient halite fluid inclusions: A screening protocol. *Gondwana Res.* 69, 163–176.

Blamey N. J. F., Brand U., Parnell J., Spear N., Lécuyer C., Benison K., Meng F. and Ni P. (2016) Paradigm shift in determining Neoproterozoic atmospheric oxygen. *Geol.* 44, 651–654.

Brand U., Davis A. M., Shaver K. K., Blamey N. J. F., Heizler M. and Lécuyer C. (2021) Atmospheric oxygen of the Paleozoic. *Earth Sci. Rev.* 216, 103560.

Bekaert, D. V., Avice, G., Marty, B. (2025) Fluid inclusions: tiny windows into global paleo-environments. *Commun. Earth Environ. 6*, 820.

Brimblecombe P. (1996) *Air Composition and Chemistry.*, Cambridge University Press.

Burke E. A. J. (2001) Raman microspectrometry of fluid inclusions. *Lithos* 55, 139–158.

Caballero R. and Huber M. (2013) State-dependent climate sensitivity in past warm climates and its implications for future climate projections. *Proc. Natl. Acad. Sci. U.S.A.* 110, 14162–14167.

Canfield D. (2013) Proterozoic Atmospheric Oxygen. *Treatise on Geochemistry: Second Edition* 6, 197–216.

Catling D. C. and Zahnle K. J. (2020) The Archean atmosphere. *Sci. Adv.* 6, eaax1420.

Caumon M.-C., Tarantola A. and Mosser-Ruck R. (2015) Raman spectra of water in fluid inclusions: I. Effect of host mineral birefringence on salinity measurement. *J. Raman Spectrosc.* 46, 969–976.

Cui Q., Chandra S. and McCahan S. (2001) The Effect of Dissolving Gases or Solids in Water Droplets Boiling on a Hot Surface. *J. Heat Transf.* 123, 719–728.

Davis A. R. and Oliver B. G. (1972) A Vibrational-Spectroscopic Study of the Species Present in the CO2-HzO System. *J. Solution Chem.* 1, 11.

Des Marais D. J. and Moore J. G. (1984) Carbon and its isotopes in mid-oceanic basaltic glasses. *EPSL* 69, 43–57.

Drever J. I. (1997) *The Geochemistry of Natural Waters: Surface and Groundwater Environments.*, Prentice Hall.

Dreybrodt W., Lauckner J., Zaihua L., Svensson U. and Buhmann D. (1996) The kinetics of the reaction $CO_2 + H_2O \rightarrow H^+ + HCO_3^-$ as one of the rate limiting steps for the dissolution of calcite in the system H_2O-CO_2-$CaCO_3$. *Geochim. Cosmochim. Acta* 60, 3375.

Fenner W. R., Hyatt H. A., Kellam J. M. and Porto S. P. S. (1973) Raman cross section of some simple gases. *J. Opt. Soc. Am., JOSA* 63, 73–77.

Foster G. L., Royer D. L. and Lunt D. J. (2017) Future climate forcing potentially without precedent in the last 420 million years. *Nat. Commun.* 8, 14845.

Fouche D. G. and Chang R. K. (1971) Relative Raman cross section for N_2, O_2, CO, CO_2, SO_2, and H_2S. *Appl. Phys. Lett.* 18, 579–580.

Frezzotti M. L., Tecce F. and Casagli A. (2012) Raman spectroscopy for fluid inclusion analysis. *J. Geochem. Explor.* 112, 1–20.

Fries M. and Steele A. (2011) Raman Spectroscopy and Confocal Raman Imaging in Mineralogy and Petrography. In *Springer Series in Optical Sciences* pp. 111–135.

Guillerm E., Lowenstein T. K., Gardien V., Brauer A., Kruger Y., Arnuk W. D., Caupin F. (2025) A physical model for accurate paleotemperature reconstruction from fluid inclusions in halite. *AJS* 325, Article 7.

Gibson M. E. and Benison K. C. (2023) It's a trap: Modern and ancient halite as Lagerstatten. *J. Sediment. Res.* 93, 642-655.

Goldstein R. H. (2001) Clues from Fluid Inclusions. *Science* 294, 1009–1011.

Graney J. R. and Kesler S. E. (1995) Factors affecting gas analysis of inclusion fluid by quadrupole mass spectrometry. *Geochim. Cosmochim. Acta* 59, 3977–3986.

He X., Wang W.-Q., Liu Y.-Z. and Sun Q. (2024) Raman Quantitative Measurement on the Cl^- Molarity of H_2O-NaCl-CO_2 System: Application to Fluid Inclusions. *Minerals* 14, 1121.

Hermann C., Dewes I. and Schumpe A. (1995) The estimation of gas solubilities in salt solutions. *Chem. Eng. Sci.* 50, 1673–1675.

Henzler K., Fetisov E. O., Galib M., Baer M. D., Legg B. A., Borca C., Xto J. M., Pin S., Fulton J. L., Schenter G. K., Govind N., Siepmann J. I., Mundy C. J., Huthwelker T. and De Yoreo J. J. (2018) Supersaturated calcium carbonate solutions are classical. *Sci Adv* 4, eaao6283.

Higgins J. A., Kurbatov A. V., Spaulding N. E., Brook E., Introne D. S., Chimiak L. M., Yan Y., Mayewski P. A. and Bender M. L. (2015) Atmospheric composition 1 million years ago from blue ice in the Allan Hills, Antarctica. *Proc. Natl. Acad. Sci.* 112, 6887–6891.

Hudgins M. N., Knobbe T. K., Hubbard J., Steele A., Park J. G. and Schaller M. F. (2024) In situ quantification of carbonate species concentrations, pH, and pCO_2 in calcite fluid inclusions using confocal Raman spectroscopy. *Appl. Spectrosc.* 00037028241275192.

Ikeda T., Fukazawa H., Mae S., Pepin L., Duval P., Champagnon B., Lipenkov V. Ya. and Hondoh T. (1999) Extreme fractionation of gases caused by formation of clathrate hydrates in Vostok Antarctic Ice. *Geophys. Res. Lett.* 26, 91–94.

Johnson K. S. (1982) Carbon dioxide hydration and dehydration kinetics in seawater. *Limnol. Oceanogr.* 27, 849–855.

Judd E. J., Tierney J. E., Lunt D. J., Montañez I. P., Huber B. T., Wing S. L. and Valdes P. J. (2024) A 485-million-year history of Earth's surface temperature. *Science* 385, eadk3705.

Kent D. V. and Muttoni G. (2013) Modulation of Late Cretaceous and Cenozoic climate by variable drawdown of atmospheric pCO_2 from weathering of basaltic provinces on continents drifting through the equatorial humid belt. *Clim. Past* 9, 525–546.

Kern D. M. (1960) The hydration of carbon dioxide. *J. Chem. Educ.* 37, 14.

Knobbe T. K. and Schaller M. F. (2018) A tight coupling between atmospheric pCO_2 and sea-surface temperature in the Late Triassic. *Geol.* 46, 43–46.

Krissansen-Totton J., Arney G. N. and Catling D. C. (2018) Constraining the climate and ocean pH of the early Earth with a geological carbon cycle model. *Proc. Natl. Acad. Sci. U.S.A.* 115, 4105–4110.

Krissansen-Totton J., Buick R. and Catling D. C. (2015) A statistical analysis of the carbon isotope record from the Archean to Phanerozoic and implications for the rise of oxygen. *Am. J. Sci.* 315, 275–316.

Krissansen-Totton J., Kipp M. A. and Catling D. C. (2021) Carbon cycle inverse modeling suggests large changes in fractional organic burial are consistent with the carbon isotope record and may have contributed to the rise of oxygen. *Geobiology* 19, 342–363.

Ku H. H. (1996) Notes on the use of propagation of error formulas. *J. Res. Natl. Bur. Stand.* 70, 263–273.

Larson T. E., Sollo F. W. and Mcgurk F. F. (1973) Complexes affecting the solubility of calcium carbonate in water. *Water Resources Research*, 1–49.

Lowenstein T. K., Timofeeff M. N., Brennan S. T., Hardie L. A. and Demicco R. V. (2001) Oscillations in Phanerozoic Seawater Chemistry: Evidence from Fluid Inclusions. *Science* 294, 1086–1088.

Lu X., Al-Qadiri H. M., Lin M. and Rasco B. A. (2011) Application of Mid-infrared and Raman Spectroscopy to the Study of Bacteria. *Food Bioprocess Technol.* 4, 919–935.

Lüthi D., Le Floch M., Bereiter B., Blunier T., Barnola J.-M., Siegenthaler U., Raynaud D., Jouzel J., Fischer H., Kawamura K. and Stocker T. F. (2008) High-resolution carbon dioxide concentration record 650,000–800,000 years before present. *Nature* 453, 379–382.

Lyons T. W., Reinhard C. T. and Planavsky N. J. (2014) The rise of oxygen in Earth's early ocean and atmosphere. *Nature* 506, 307–315.

McDonald J. H. (2014) *Handbook of biological statistics*., Sparky House Publishing.

McElwain J. C., Beerling D. J. and Woodward F. I. (1999) Fossil Plants and Global Warming at the Triassic-Jurassic Boundary. *Science* 285, 1386–1390.

McSween H. Y., Richardson S. M. and Uhle M. E. (2003) *Geochemistry: Pathways and Processes*. 2nd ed., Columbia University Press.

Mills B. J. W., Krause A. J., Jarvis I. and Cramer B. D. (2023) Evolution of Atmospheric O_2 Through the Phanerozoic, Revisited. *Annu. Rev. Earth Planet Sci.* 51, 253–276.

Mißbach H., Duda J.-P., van den Kerkhof A. M., Lüders V., Pack A., Reitner J. and Thiel V. (2021) Ingredients for microbial life preserved in 3.5 billion-year-old fluid inclusions. *Nat. Commun.* 12, 1101.

Mullin J. W. (2001) *Crystallization*., Elsevier Science & Technology, Chantilly, United Kingdom.

Norman D. I., Blamey N. J. F. (2001) Quantitative analysis of fluid inclusion volatiles by a quadrupole mass spectrometer system. *ECROFI* 7, 341-344.

Ohno H., Iizuka Y. and Fujita S. (2021) Pure rotational Raman spectroscopy applied to N_2/O_2 analysis of air bubbles in polar firn. *J. Glaciol.* 67, 903–908.

Onda K., Sada E., Kobayashi T., Kito S. and Ito K. (1970) Salting-out parameters of gas solubility in aqueous salt solutions. *J. Chem. Eng. Japan* 3, 18–24.

Park J. G. and Schaller M. F. (2025) Constraints on Earth's atmospheric evolution from a gas-aqueous partition of fluid inclusion volatiles. *Gondwana Res.* 139, 204–215.

Park J. G., Hudgins M. N., Fralick P., Shelley J. T., and Schaller M. F. (2025) Breathing life into the boring billion: Direct constraints from 1.4 Ga fluid inclusions reveal a fair climate and oxygenated atmosphere. *PNAS* 122, e2513030122.

Petit J. R., Jouzel J., Raynaud D., Barkov N. I., Barnola J.-M., Basile I., Bender M., Chappellaz J., Davis M., Delaygue G., Delmotte M., Kotlyakov V. M., Legrand M., Lipenkov V. Y., Lorius C., PÉpin L., Ritz C., Saltzman E. and Stievenard M. (1999) Climate and atmospheric history of the past 420,000 years from the Vostok ice core, Antarctica. *Nature* 399, 429–436.

Pettitt E. A., Cherniak D. J., Schaller M. F. and Watson E. B. (2020) Diffusive retention of carbon and nitrogen in a microcrystalline quartz-dominated chert: Implications for reconstructing Earth's ancient atmosphere. *Chem. Geol.* 541, 119572.

Pettitt E. A. and Schaller M. F. (2020) A new calibration technique for quantitative gas analyses of fluid inclusions using a quadrupole mass spectrometer. *RCM* 34.

Pretet C., Reynaud S., Ferrier-Pagès C., Gattuso J.-P., Kamber B. S. and Samankassou E. (2014) Effect of salinity on the skeletal chemistry of cultured scleractinian zooxanthellate corals: Cd/Ca ratio as a potential proxy for salinity reconstruction. *Coral Reefs* 33, 169–180.

Royer D. L. (2014) Atmospheric CO_2 and O_2 During the Phanerozoic: Tools, patterns, and impacts. In *Treatise on Geochemistry* Elsevier. pp. 251–267.

Schaller M. F., Wright J. D. and Kent D. V. (2015) A 30 Myr record of Late Triassic atmospheric pCO_2 variation reflects a fundamental control of the carbon cycle by changes in continental weathering. *Geol. Soc. Am. Bull.* 127, 661–671.

Schaller M. F., Wright J. D. and Kent D. V. (2011) Atmospheric pCO_2 perturbations associated with the Central Atlantic Magmatic Province. *Science* 331, 1404–1409.

Schreder-Gomes S. I., Benison K. C. and Bernau J. A. (2022) 830-million-year-old microorganisms in primary fluid inclusions in halite. *Geol.* 50, 918–922.

Severinghaus J. P. and Battle M. O. (2006) Fractionation of gases in polar ice during bubble close-off: New constraints from firn air Ne, Kr and Xe observations. *EPSL* 244, 474–500.

Smart K. E., Breecker D. O., Blackwood C. B., Gallagher T. M. (2025) A new approach to continuous monitoring of carbon use efficiency and biosynthesis in soil microbes from measurement of CO_2 and O_2. *BG.* 22, 87-101.

Steadman J. A., Large R. R., Blamey N. J., Mukherjee I., Corkrey R., Danyushevsky L. V., Maslennikov V., Hollings P., Garven G., Brand U. and Lécuyer C. (2020) Evidence for elevated and variable atmospheric oxygen in the Precambrian. *Precambrian Res.* 343, 105722.

Sun Q. (2009) The Raman OH stretching bands of liquid water. *Vib. Spectrosc.* 51, 213-217.

Sun Q., Zhao L., Li N. and Liu J. (2010) Raman spectroscopic study for the determination of Cl^- concentration (molarity scale) in aqueous solutions: Application to fluid inclusions. *Chem. Geol.* 272, 55–61.

The Cenozoic CO_2 Proxy Integration Project (CenCO_2PIP) Consortium*†, Hönisch B., Royer D. L., Breecker D. O., et al. (2023) Toward a Cenozoic history of atmospheric CO_2. *Science* 382, eadi5177.

Tierney J. E., Poulsen C. J., Montañez I. P., et al. (2020) Past climates inform our future. *Science* 370, eaay3701.

Van Eldik R. and Palmer D. A. (1982) Effects of pressure on the kinetics of the dehydration of carbonic acid and the hydrolysis of CO_2 in aqueous solution. *J. Solution Chem.* 11, 339–346.

Vreeland R. H., Rosenzweig W. D. and Powers D. W. (2000) Isolation of a 250-million-year-old halotolerant bacterium from a primary salt crystal. *Nature* 407, 897–900.

Wang M., Zhao Y., Li W., and Liu C. (2018) Fluid inclusions in surface-temperature halite: Sample preparation and application. *Acta Geol. Sin. 92, 1592-1597.*

Williams A. E. (1996) Mass spectrometric analysis of volatiles in fluid inclusions: aliquot calibration valve to simulate inclusion rupture. *Chem. Geol.* 131, 155–165.

Yan Y., Bender M. L., Brook E. J., Clifford H. M., Kemeny P. C., Kurbatov A. V., Mackay S., Mayewski P. A., Ng J., Severinghaus J. P. and Higgins J. A. (2019) Two-million-year-old snapshots of atmospheric gases from Antarctic ice. *Nature* 574, 663–666.

Yeung L. Y. (2017) Low oxygen and argon in the Neoproterozoic atmosphere at 815 Ma. *EPSL* 480, 66–74.

Zeebe R. E. and Wolf-Gladrow D. (2001) *CO_2 in Seawater: Equilibrium, Kinetics, Isotopes*., Gulf Professional Publishing.

Zimmermann J. L. and Moretto R. (1996) Release of water and gases from halite crystals. *Eur. J. Mineral.* 8, 413–422.

Figures and Tables

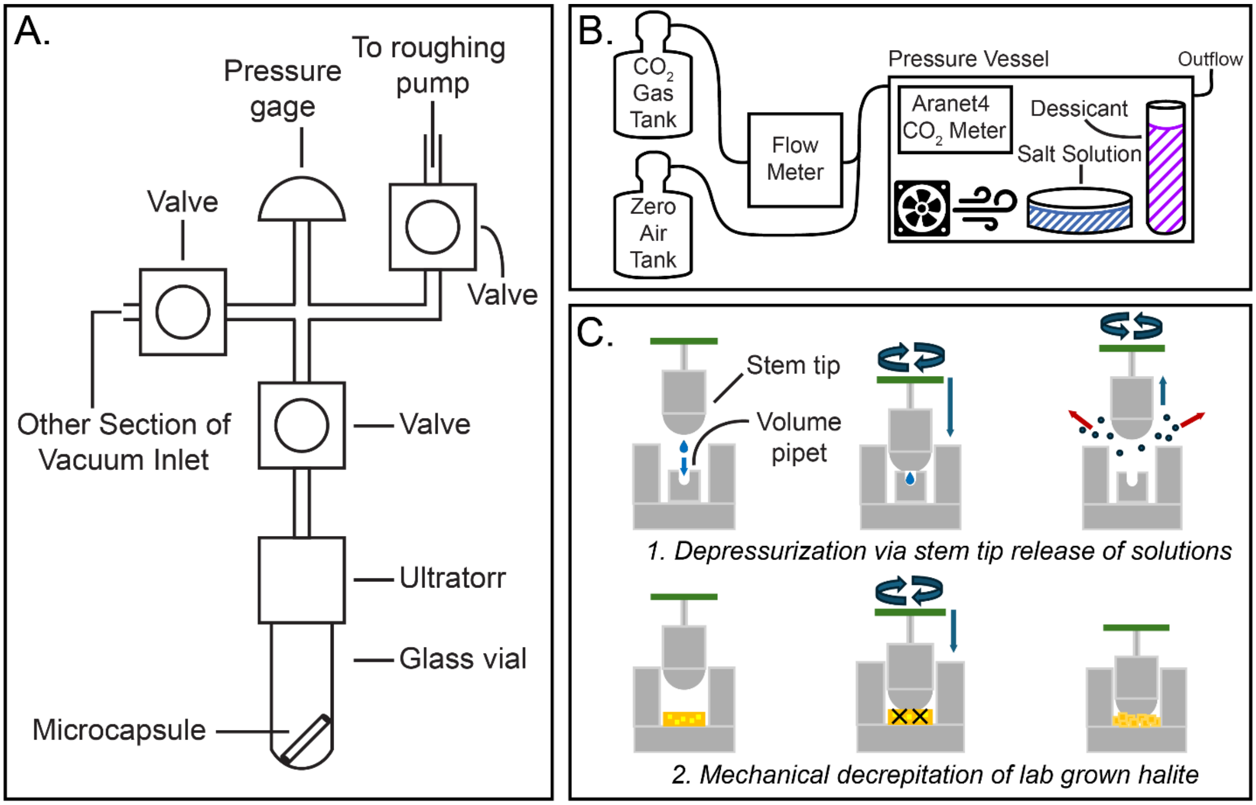

Figure 1. Experimental procedure in this study. (A) Low vacuum (10^{-3} mbar) depressurization experiment setup for the 25 and 2 µL of 0.25 M $NaHCO_3$. Video for the low-vacuum depressurization experiment is linked to the "data availability" section of the online version. Note the decrepitation time is rapid (~5 ms). (B) Experimental pressure vessel setup for growing halite in an elevated P_{CO2} environment. The vessel was held at 1 atm. (C) Schematic of stock solution depressurization and lab-grown halite decrepitation experimental procedure conducted under high vacuum on the quadrupole MS inlet line. (C-1) Volatiles were quantified via a stem tip release of the stock solutions placed inside a stainless steel volume pipet (see Pettit and Schaller, 2020). (C-2) Volatiles in the inclusions of the lab-grown halite were quantified via mechanical decrepitation, releasing the entrapped volatiles from the inclusions.

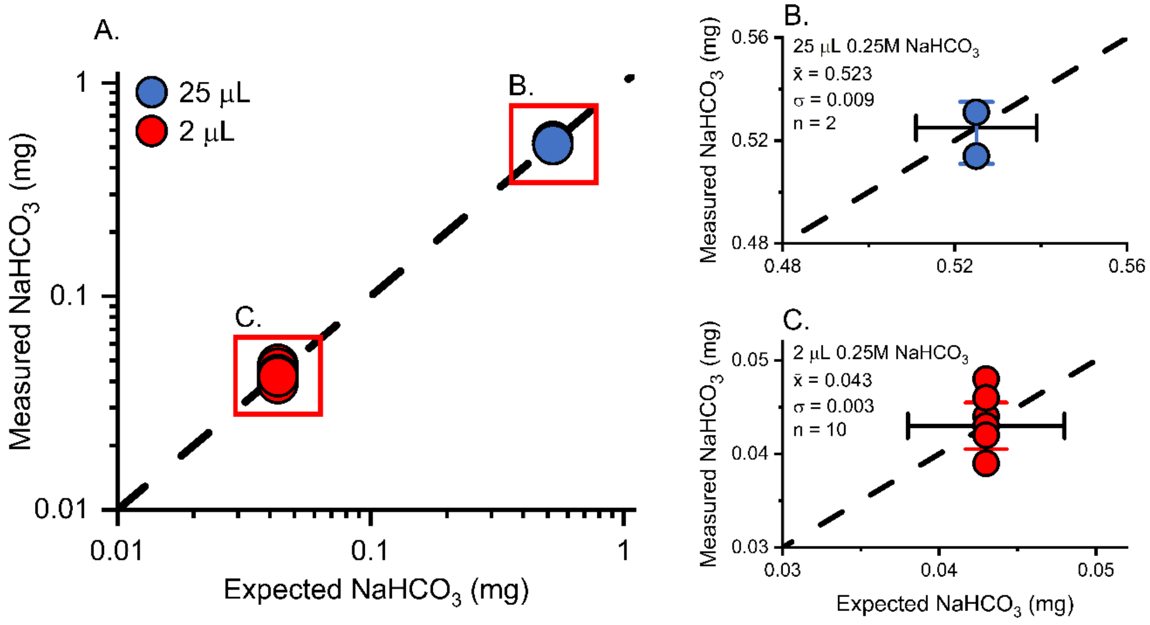

Figure 2. Mass of the expected residual $NaHCO_3$ (mg) vs mass of the measured residual $NaHCO_3$ (mg) from the low-vacuum depressurization experiments on the 0.25 M $NaHCO_3$ solution at 25 μL and 2 μL volumes (A). Dotted line is the 1:1 for the expected vs measured mass of the $NaHCO_3$ residue. Red boxes are the expanded areas for 25 μL (B) and 2 μL (C). X-axis error bars are the syringe procedural volume error and colored y-axis error bars (blue and red) are the standard deviation of the measured samples.

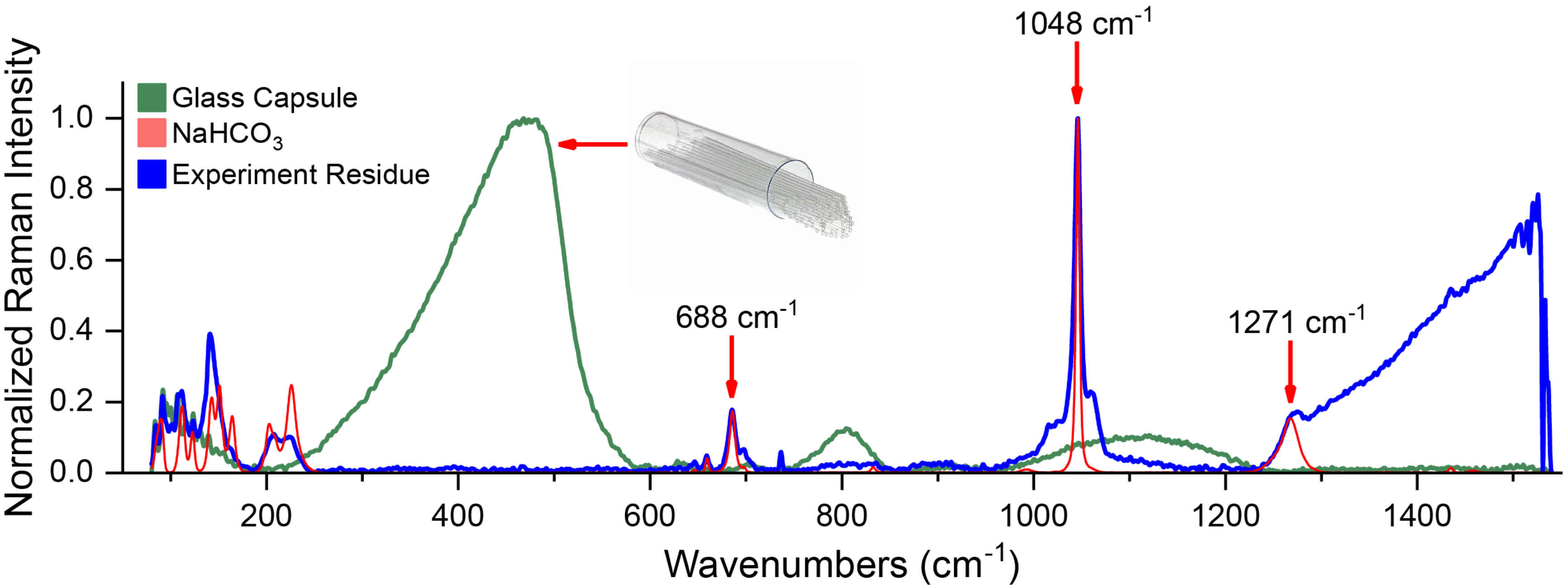

Figure 3. Raman spectra of the residue from the low-vacuum depressurization experiments. The main bands for the $NaHCO_3$ salt are at 688, 1048, and 1271 cm^{-1} (pink). The spectrum of the experimental residue spectra (blue) are similar to the spectrum of the original $NaHCO_3$ salt, confirming the experiment residue is the original carbonate salt and is distinctly different from the spectrum of the glass microcapsule (green).

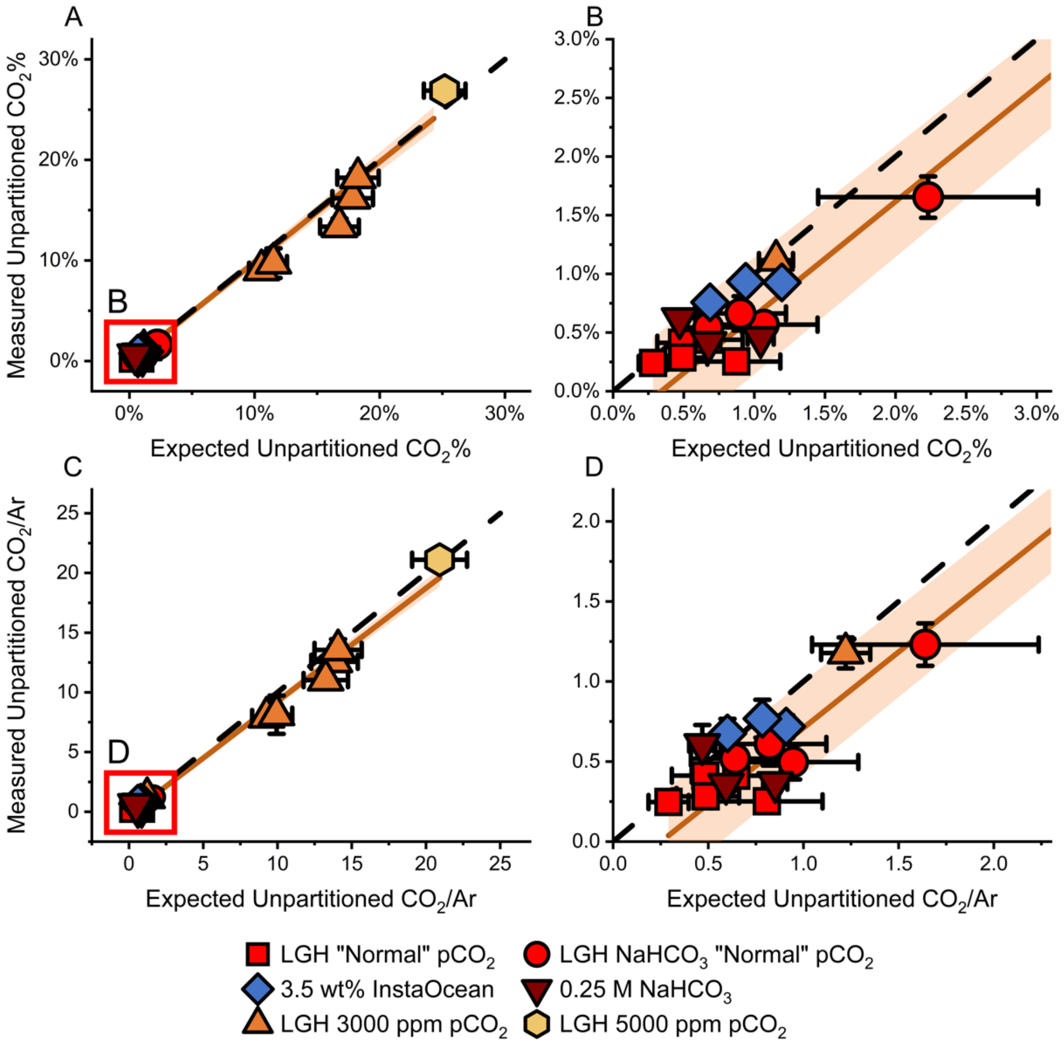

Figure 4. Results from the QMS measurements of depressurization and decrepitation experiments on the lab-grown halite (LGH) and the stock solutions. Expected vs measured CO_2 mol% (A-B) and normalized to argon (C-D) before partitioning between the aqueous and gaseous contributions. Red boxes are the expanded areas of the measured unpartitioned CO_2 mol% (B) and argon normalized CO_2 (D). Dashed line is the 1:1 of an air and air-saturated brine CO_2 mix, and the solid brown line is the linear relationship between measured and expected. Color-shaded areas are 95% confidence intervals. The error bars on the expected CO_2 were estimated based on the gas volume fraction and the range of CO_2 that the stock solutions and LGH were equilibrated under. The error bars on the measured CO_2 content are propagated uncertainties at the 95% confidence interval.

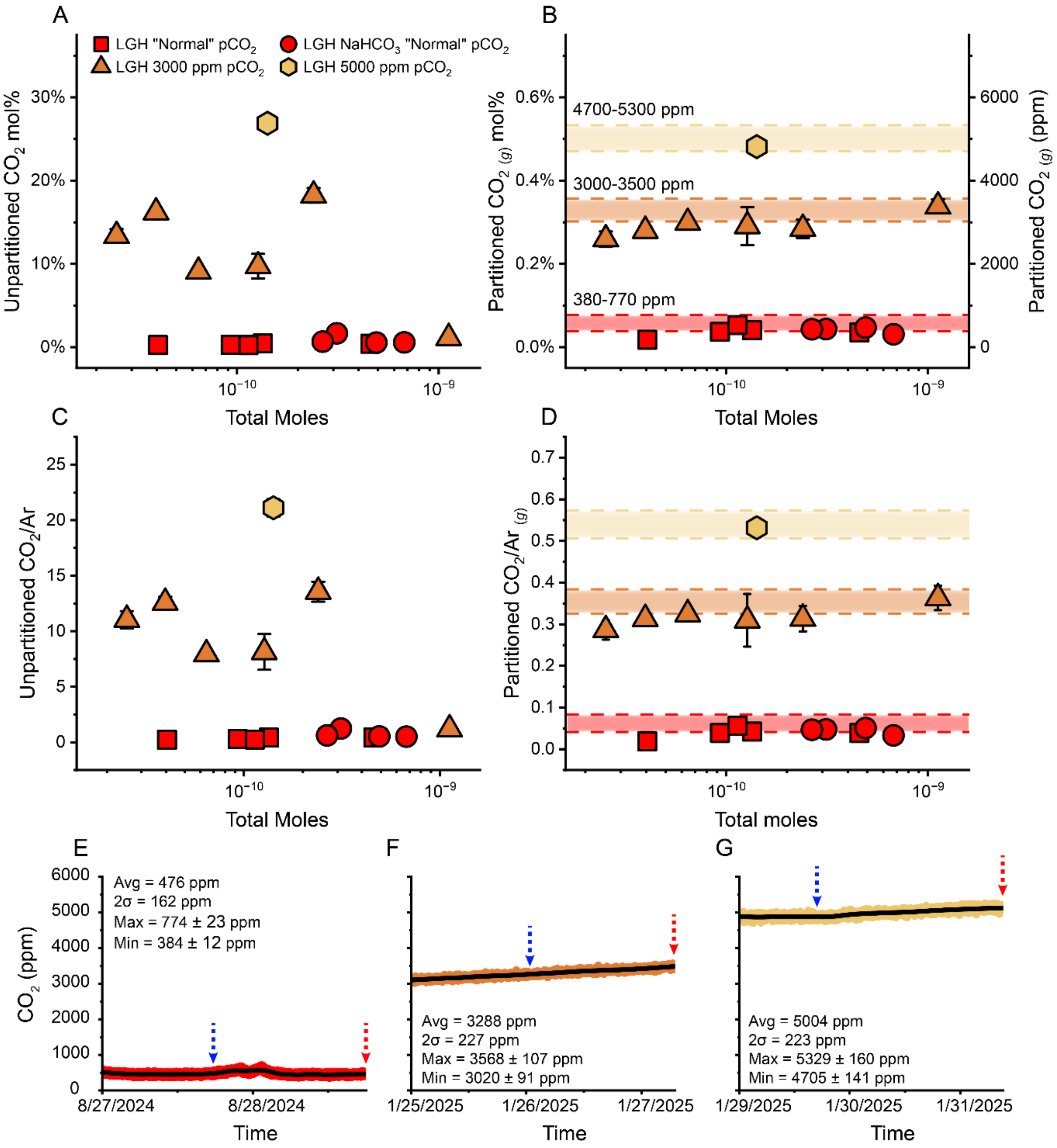

Figure 5. Total moles of measured gas (e.g., the sum of N_2, O_2, Ar, CO_2) versus the unpartitioned (A, C) and partitioned (B, D) CO_2 mol% and argon normalized CO_2 results from measurements of the lab-grown halite (LGH) decrepitation experiments. MAGPI was used to partition the raw inclusion data (Park and Schaller, 2025). Gas partitioned CO_2 measurements are compared to the monitored P_{CO2} levels. LGH precipitated under "normal" (red, E) and elevated to 3000 ppm, (orange, F) and 5000 ppm (yellow, G) conditions. Blue vertical arrows represent the time points when hopper crystals were first observed during halite precipitation and red vertical arrows represent the time points when halite crystals were collected. Note that the LGH tracks the CO_2 concentration of the atmosphere with which the solutions were equilibrated and that partitioning of inclusion data is necessary for accurate interpretations. The error bars are propagated uncertainties.

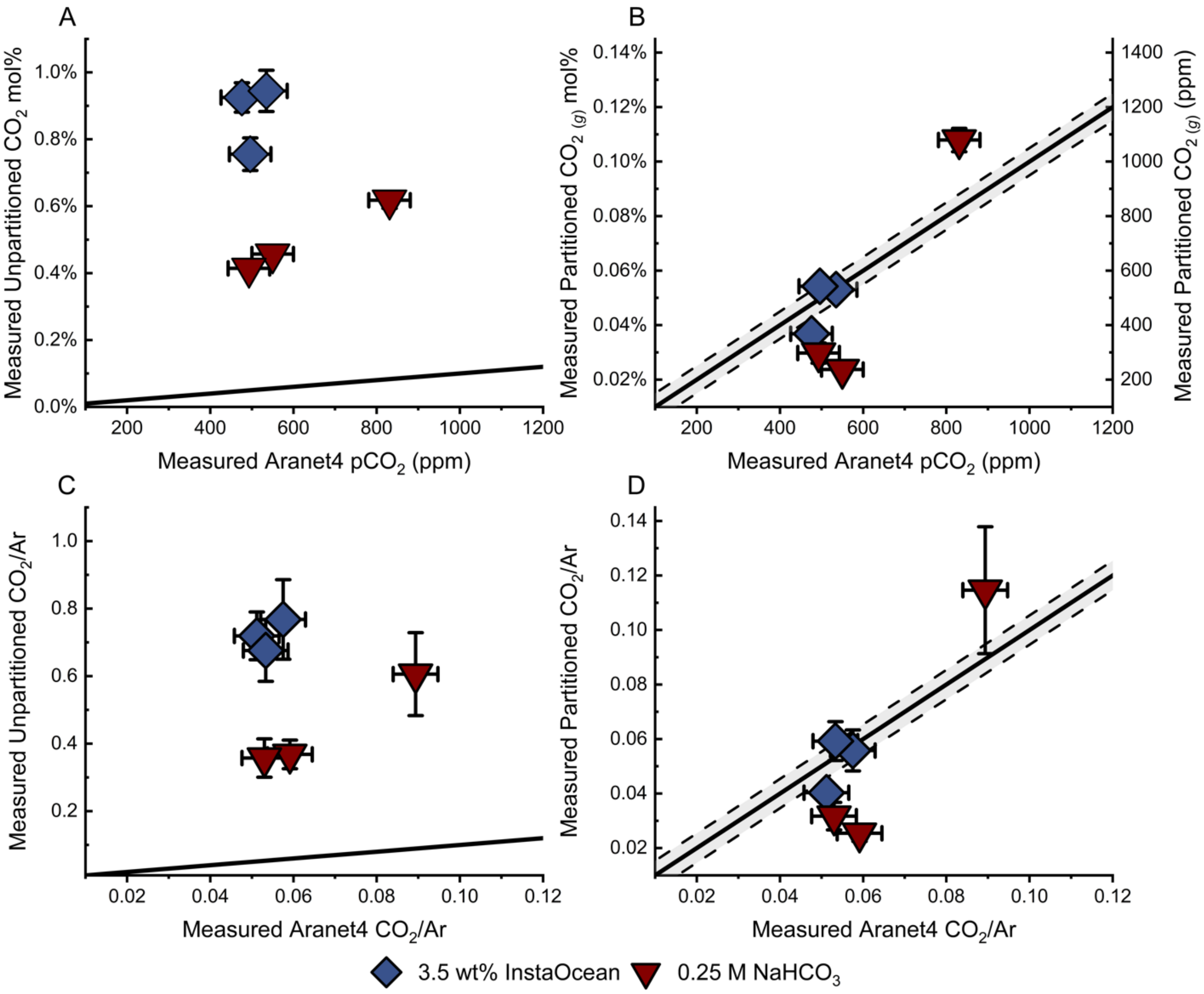

Figure 6. Measured P_{CO2} (ppm) under which the solutions equilibrated vs. the unpartitioned (A, C) and partitioned (B, D) CO_2 mol% or CO_2/Ar from the solution depressurization experiments. The P_{CO2} was measured by the Aranet4 CO_2 meter before the setup of each stock solution depressurization experiment. The argon to which the CO_2 was normalized was assumed to be at 0.93% in the laboratory. The solid black line is the 1:1 between the Aranet4 measured CO_2 and the QMS measured CO_2 mol% and CO_2/Ar. Dashed lines and grey shaded area are the error associated with the uncertainty in the Aranet4 CO_2 measurements at this range (± 3%). The unpartitioned CO_2 noticeably diverges from the 1:1 line. However, the data partitioned using MAGPI (Park and Schaller, 2025) closely aligns with the 1:1 line. X-axis error is the CO_2 error of the Aranet4 and the y-axis error are propagated uncertainties.

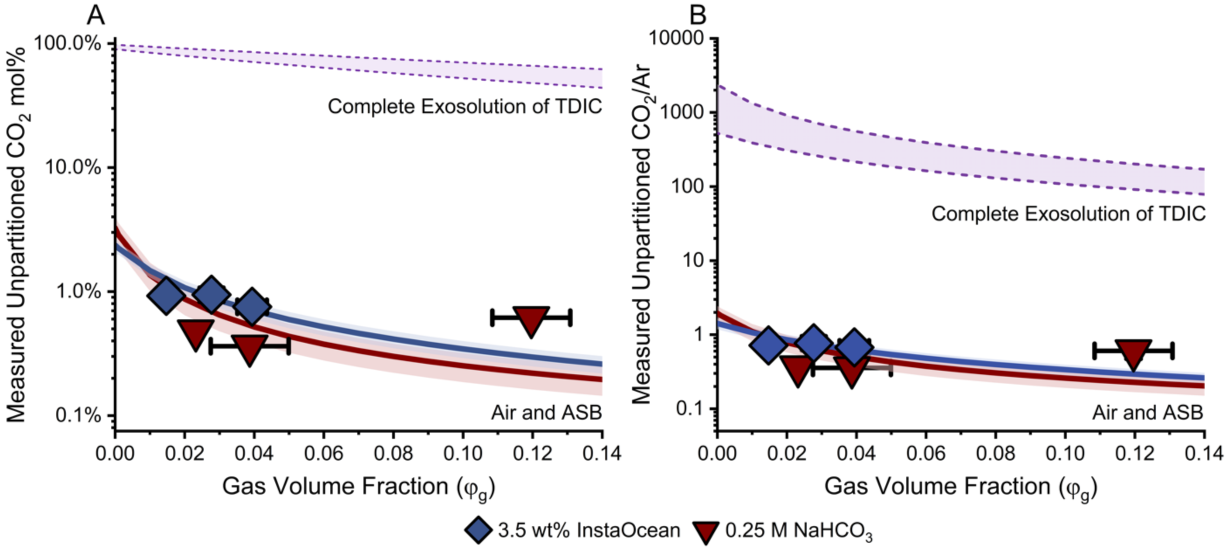

Figure 7. Results from the depressurization experiments. Measured gas volume fraction vs unpartitioned CO_2 mol% (log scale) (A) and argon normalized (B) on the 3.5 wt% InstaOcean (diamonds) and 0.25 M $NaHCO_3$ (inverted triangles) solutions. Solid blue and burgundy lines are the modeled expected values if the measured CO_2 represents a mix between air and air-saturated brine (ASB) for a NaCl and $NaHCO_3$ dominated solutions, respectively. Shaded blue and burgundy areas are the associated error for each air and ASB model. The upper and lower dotted purple lines are the model values where the measured CO_2 represents the complete exsolution of total dissolved inorganic carbon (TDIC) for a NaCl and $NaHCO_3$ dominated solution, respectively. The measured CO_2 content aligns with the expected for an air-ASB mixture. Note the prominent difference between the modeled complete exsolution of TDIC and the actual measured CO_2. X- and Y-axis error bars are the propagated uncertainty for the gas volume fraction and the measured CO_2, respectively.

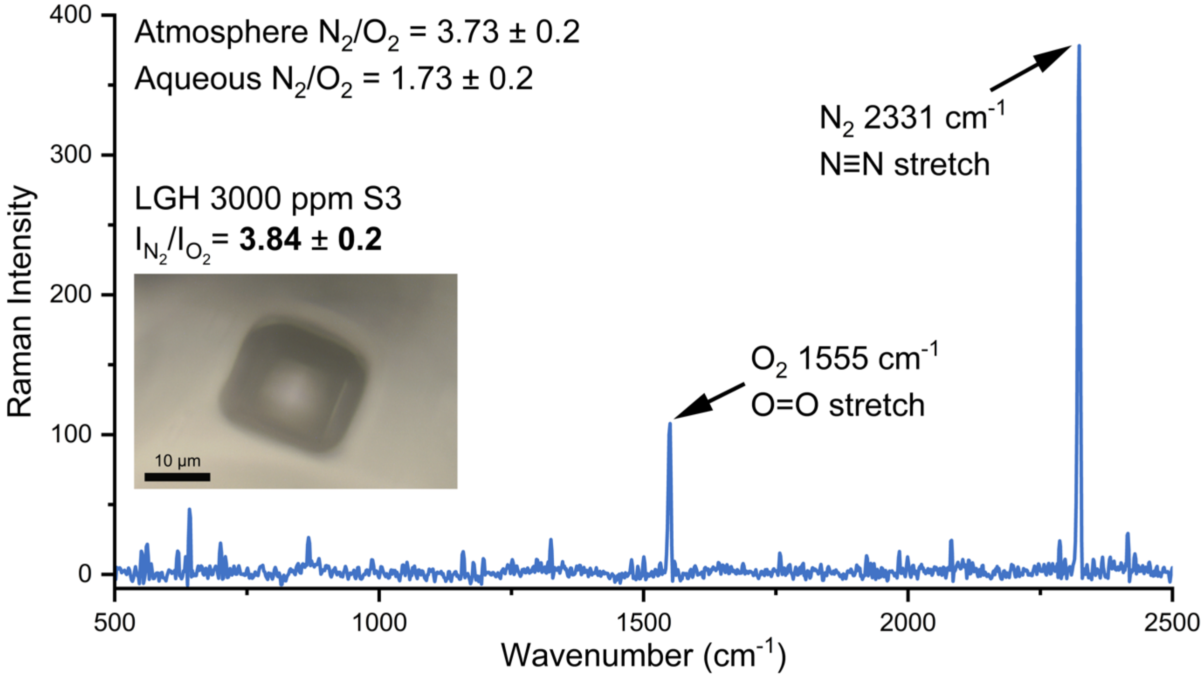

Figure 8. Raman spectrum of a fluid inclusion gas bubble in the lab-grown halite (LHG) that precipitated in ‘zero air’ (nominal atmospheric ratio of N_2, O_2 and Ar) with a maximum P_{CO2} level of 3568 ± 107 and minimum P_{CO2} of 3020 ± 91 ppm. The main N_2 and O_2 peaks are present at 2331 and 1555 cm^{-1}, respectively. The ratio between the intensities of the N_2 and O_2 peaks (3.84 ± 0.2) closely matches the gaseous N_2/O_2 endmember (3.73 ± 0.2) under which the LGH precipitated and does not overlap with the aqueous N_2/O_2 endmember (1.73 ± 0.2).

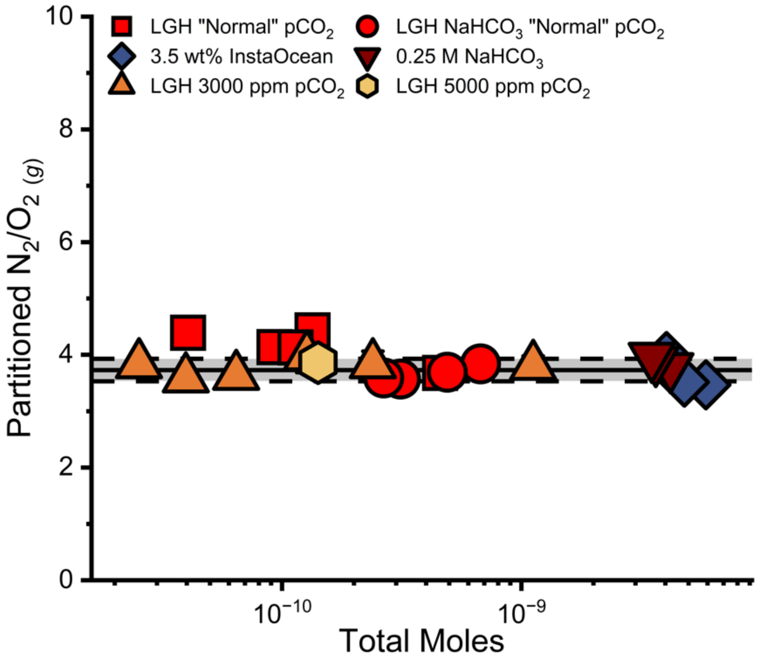

Figure 9. Partitioned $N_{2\,(g)}$ normalized to $O_{2\,(g)}$ results from the stock solution depressurization and the lab-grown halite (LGH) decrepitation experiments vs. total moles (sum of the measured N_2, O_2, Ar, and CO_2). Partitioned N_2/O_2 ratio of measurements is compared to the expected N_2/O_2 of the atmosphere under which the stock solutions and LGH equilibrated (solid black line). Dashed black lines and grey shaded area are the error range of N_2/O_2 for LGH precipitation. Stock solutions were equilibrated in open laboratory air and assumed N_2 was 78.08% and O_2 was 20.95%. Note that data converges to the atmospheric N_2/O_2 value (3.73 ± 0.2). Error bars are the propagated uncertainties.

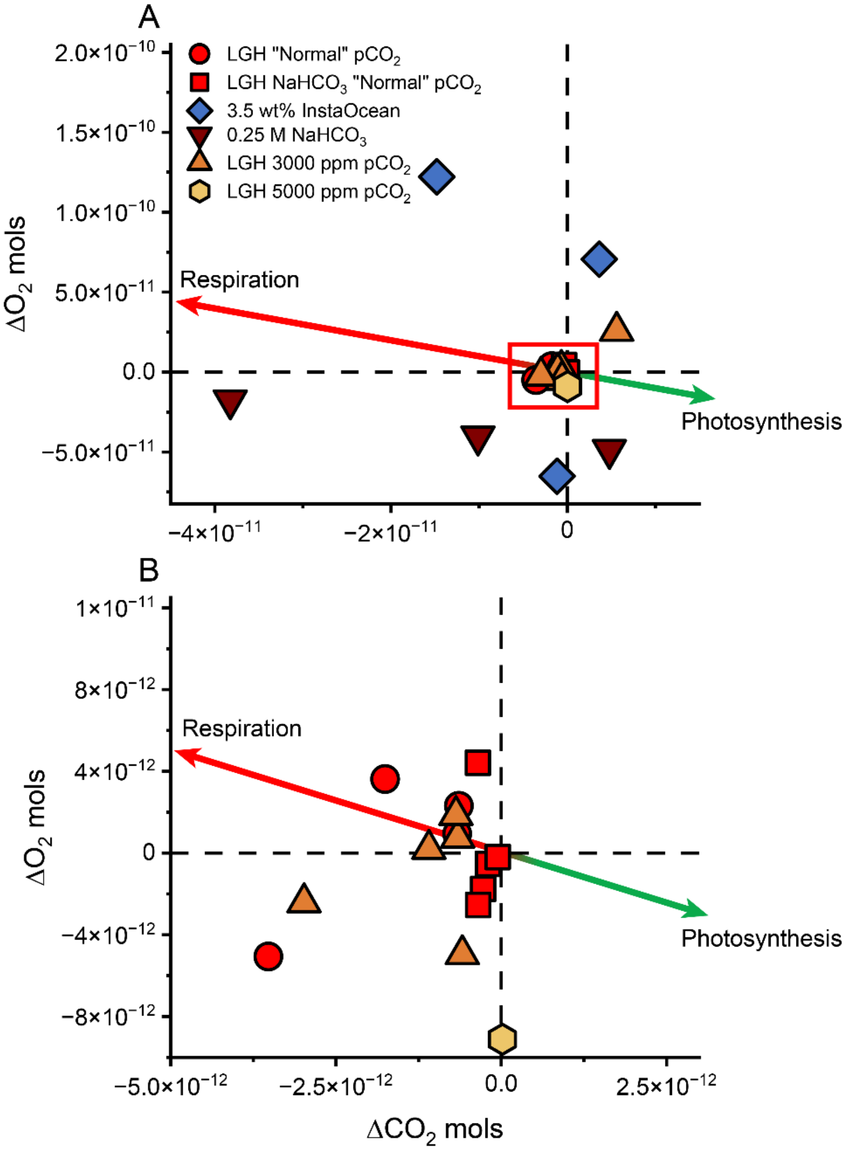

Figure 10. (A) Difference between measured and expected moles of CO_2 and O_2 in the stock solutions and lab-grown halite (LGH). Delta values are calculated relative to the samples respective atmospheric ratio using equation (6). (B) The expanded area of the red box in A. Green and red lines are the 1:1 expectation for stoichiometric exchange by photosynthesis and respiration, respectively. Black dashed lines represent the origin.

Table 1. Forward and reverse kinetic reaction rate constants for Eq. 1a-f

Reaction	Reaction direction	magnitude	Reference
Eq. 1a	k_{+1}	$1.6\text{x}10^{-5}$ s^{-1}	calculated
	k_{-1}	$4.1\text{x}10^{-4}$ s^{-1}	Choi et al. (1998)
Eq. 1b	k_{+2}	$1\text{x}10^{4}$ $M^{-1}\cdot s^{-1}$	Eigen et al. (1961)
	k_{-2}	18.3 s^{-1}	Eldik and Palmer (1982)
Eq. 1c	k_{+3}	Instantaneously	Kern (1960)
	k_{-3}	Instantaneously	Kern (1960)
Eq. 1d	k_{+4}	59.4 s^{-1}	Zeebe and Wolf-Gladrow (2001)
	k_{-4}	$5\text{x}10^{10}$ $M^{-1}\cdot s^{-1}$	Eigen et al. (1961)
Eq. 1e	k_{+5}	0.037 s^{-1}	Johnson (1982)
	k_{-5}	$2.66\text{x}10^{4}$ $M^{-1}\cdot s^{-1}$	Zeebe and Wolf-Gladrow (2001)
Eq. 1f	k_{+6}	$4.05\text{x}10^{3}$ $M^{-1}\cdot s^{-1}$	Johnson (1982)
	k_{-6}	$1.76\text{x}10^{-4}$ s^{-1}	Zeebe and Wolf-Gladrow (2001)

Table 2. Measured mass of the residue from the low-vacuum depressurization experiments compared to the residue mass expected from the syringe on the 0.25 M $NaHCO_3$ solutions at 2 and 25uL.

0.25M $NaHCO_3$	Measured Residue (mg)	Syringe Procedural Range (mg)
2 µL (n=10)	0.043 ± 0.003	0.043 ± 0.003
25 µL (n=2)	0.523 ± 0.009	0.525 ± 0.014

Table 3. Correlations between the measured vs. expected unpartitioned CO_2 mol% and CO_2/Ar, and ANOVA and ANCOVA results with F-test and associated p-value of the measured unpartitioned CO_2 mol% and CO_2/Ar compared to the 1:1. Bolded values are significant.

	Equation	**R²**	**ANOVA**		**ANCOVA**		***Homogeneity of regression***	
			F	p(α)	F	p(α)	***F***	***p(α)***
Unpartitioned CO_2 mol%	y=0.97x-0.003	0.98	0.041	0.84	5.02	0.03	0.13	0.72
Unpartitioned CO_2/Ar	y=0.95x-0.24	0.99	0.06	0.80	12.46	0.01	4.21	0.05

Table 4. Comparisons between the average and standard deviation of the CO_2 content before and after applying the gas-aqueous partition to lab-grown halite (LGH). Partitioned compositions closely match the compositions under which the LGH equilibrated.

Samples	CO_2 mol%	CO_2/Ar
LGH “Normal” P_{CO_2} (n=5)		
Unpartitioned	0.3305 ± 0.0973	0.3156 ± 0.0906
Partitioned	0.0367 ± 0.0127	0.0387 ± 0.0134
LGH $NaHCO_3$ “Normal” P_{CO_2} (n=4)		
Unpartitioned	0.8574 ± 0.5338	0.7140 ± 0.3480
Partitioned	0.0410 ± 0.0070	0.0443 ± 0.0078
LGH ~3000 ppm P_{CO_2} (n=6)		
Unpartitioned	11.2851 ± 6.1200	9.0663 ± 4.4880
Partitioned	0.2918 ± 0.0263	0.3183 ± 0.0253
LGH ~5000 ppm P_{CO_2} (n=1)		
Unpartitioned	26.8913	21.1087
Partitioned	0.4816	0.5316
Aranet4 CO_2	**Minimum**	**Maximum**
LGH “Normal” P_{CO_2}	0.0384 ± 0.0012	0.0774 ± 0.0023
LGH ~3000 ppm P_{CO_2}	0.3020 ± 0.0091	0.3568 ± 0.0107
LGH ~5000 ppm P_{CO_2}	0.4705 ± 0.0141	0.5329 ± 0.0160

Table 5. Comparisons between the average and standard deviation of the CO_2 content of stock solutions both before and after applying the gas-aqueous partition. Partitioned compositions closely match the compositions in which the stock solutions equilibrated under.

Samples	CO_2 mol%	CO_2/Ar
3.5 wt% InstaOcean (n=3)		
Unpartitioned	0.8729 ± 0.0999	0.7211 ± 0.0460
Partitioned	0.0480 ± 0.0096	0.0518 ± 0.0101
0.25 M $NaHCO_3$ (n=3)		
Unpartitioned	0.4963 ± 0.1074	0.4439 ± 0.1405
Partitioned	0.0538 ± 0.0470	0.0573 ± 0.0498